Applied Surface Science 721 (2026) 165446

Contents lists available at ScienceDirect

Applied Surface Science

journal homepage: www.elsevier.com/locate/apsusc

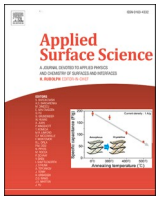

Full Length Article

Surface-engineered Ag/TiO_2/graphitic carbon nitride nanocomposites on cotton textiles for multifunctional photocatalytic, UV shielding, and antibacterial performance

Dominika Glažar [a], Brigita Tomšič [a], Ivan Jerman [b], Raghuraj S. Chouhan [c], Andraž Šuligoj [b,d], Matija Zorc [a], Albin Pintar [b], Janez Kovač [c], Andraž Krajnc [b], Francisco Ruiz-Zepeda [b], Barbara Simončič [a,*]

[a] Faculty of Natural Sciences and Engineering, University of Ljubljana, Aškerčeva Cesta 12, 1000 Ljubljana, Slovenia
[b] National Institute of Chemistry, Hajdrihova 19, 1001 Ljubljana, Slovenia
[c] Jožef Stefan Institute, Jamova Cesta 39, 1000 Ljubljana, Slovenia
[d] Faculty of Chemistry and Chemical Technology, University of Ljubljana, Večna Pot 113, 1000 Ljubljana, Slovenia

ARTICLE INFO

Keywords:
Textile
Multifunctional
Nanocomposites
g-C_3N_4
Titanium dioxide
Silver

ABSTRACT

Ternary noble metal/semiconductor heterostructures are emerging as versatile platforms for multifunctional materials, but their integration into textiles remains limited. In this study, ultrasound-assisted sol–gel synthesis of Ag/TiO_2/graphitic carbon nitride (gCN) nanocomposites directly on cotton fabric was developed. Two synthesis routes, i.e. *in situ* and *ex situ* were carried out at 20 °C and 70 °C to simultaneously achieve photocatalytic, UV protection, and antimicrobial properties. *In situ* synthesis at 70 °C resulted in the highest loading of TiO_2 and Ag nanoparticles (NPs), leading to superior multifunctional performance. The enhanced photocatalytic activity and photostability of the nanocomposite under solar light irradiation were attributed to a Type-II heterojunction between TiO_2 and gCN, the Schottky barrier formation at the Ag/TiO_2 interface, and the localised surface plasmon resonance of the Ag NPs. The synergistic effect of gCN and Ag NPs on UV-A absorption combined with TiO_2-mediated UV-B shielding resulted in a UV protection factor of 90. The dual effect of Ag^+ and Ag^0 species provided complete bacterial inactivation of *S. aureus* and *E. coli*. The level of Ag NPs remained below the cytotoxic threshold, ensuring excellent cytocompatibility. These results establish Ag/TiO_2/gCN nanocomposite-functionalised cotton as a promising candidate for advanced biomedical and technical textile applications.

1. Introduction

Rapid progress in the synthesis of nanomaterials with different chemical structures, morphologies, and dimensions has significantly influenced the processes relating to the chemical modification of textiles and has facilitated the development of advanced textile nanocomposites [1,2]. Due to their large specific surface area and the quantum effect, which is reflected in their high chemical reactivity; unique optical, electrical, and magnetic properties; high strength; and physicochemical resistance, nanomaterials have almost completely replaced conventional chemical agents, endowing textiles with new functional properties [2,3]. As a result, their applications have expanded to various fields, including personal protection, medical textiles, pollutant degradation, filtration, wearable electronics, solar cells, and sensors [1,2]. However, the integration of nanomaterials into textiles as a means of achieving certain functional properties does not always fall in line with the principles of a sustainable approach to chemical functionalisation, which advocate for the implementation of green chemistry. According to these principles, only nanomaterials with chemically safe structures and concentrations that pose a minimal risk to human health and the environment should be used [2,3].

To achieve the multifunctional properties of textiles, various nanomaterials have been intensively investigated, including metal nanoparticles (NPs) such as silver (Ag), gold (Au), and copper (Cu); metal and metalloid oxides and hydroxides, such as titanium dioxide (TiO_2), zinc oxide (ZnO), aluminium hydroxide ($Al(OH)_3$), and silicon dioxide (SiO_2); and carbon-based nanomaterials, including graphene, graphene oxide, carbon nanotubes, and graphitic carbon nitride (gCN) [4–7]. Ag

* Corresponding author.
E-mail address: barbara.simoncic@ntf.uni-lj.si (B. Simončič).

https://doi.org/10.1016/j.apsusc.2025.165446
Received 29 September 2025; Received in revised form 20 November 2025; Accepted 30 November 2025
Available online 1 December 2025

NPs are commonly used for the functionalisation of textile fibres due to their strong antimicrobial activity against a variety of microorganisms, including bacteria, viruses, fungi, moulds, yeasts, and algae. However, the use of Ag NPs in antimicrobial textiles poses a critical challenge, as Ag NPs exhibits cytotoxic effects at the concentrations required for effective antimicrobial activity [8]. To mitigate this problem, strategies aimed at increasing antimicrobial efficacy while maintaining the Ag NPs concentration below the cytotoxicity threshold are essential. This can be achieved by using Ag NPs in combination with other active components.

Among the metal oxides, TiO_2, which is often referred to as the "golden" photocatalyst, is the most commonly used material that imparts multifunctional properties to textiles and decolourises textile wastewater. TiO_2 is an inorganic semiconductor known for its high photocatalytic activity, chemical stability, inertness, biocompatibility, non-toxicity, high refractive index, and low-cost production [4,5,9–12]. TiO_2 has been widely used as a multifunctional nanomaterial in the chemical modification of textiles, enabling photocatalytic self-cleaning, antimicrobial activity, UV protection, electrical conductivity, antistatic properties, and the increased thermal stability of textile fibres [5]. However, a major limitation of TiO_2 results from its wide band gap (~3.2 eV for anatase), which restricts its photocatalytic activity to the UV region of the spectrum. Various strategies have been explored to improve photocatalytic activity in the visible light region, including metal doping and the formation of coupled semiconductor systems that have a smaller band gap [5,13].

As a sustainable next-generation carbon-based photocatalyst, gCN has attracted considerable attention in recent years due to its unique optical and electronic properties, high physicochemical and thermal stability, excellent corrosion resistance, and low-cost production [7,14,15]. It is an organic, two-dimensional conjugated polymer semiconductor that has a graphite-like layered structure consisting of s-triazine and tri-s-triazine, with the layers being held together by van der Waals forces [7]. gCN has effectively replaced conventional inorganic semiconductors in various fields such as environmental remediation, fuel production, energy conversion and storage, and biomedical applications [16–23]. Its relatively narrow band gap (~2.7 eV) enables photocatalytic activity under solar light illumination up to about 460 nm [24,25]. However, its practical photocatalytic efficiency is limited by the low charge carrier mobility and the fast recombination of the photogenerated electron-hole pairs [7,16,26]. To overcome this drawback, various morphological modifications, including the development of layered nanoparticles, have been employed to improve its photocatalytic performance [14,27,28]. In addition, strategies such as the metal doping of gCN, as well as the construction of heterojunctions with other semiconductors, including TiO_2, have been explored to enhance charge separation and broaden the absorption spectrum, thereby improving its overall photocatalytic performance [29–31].

The research carried out to date has shown that all three nanomaterials—Ag NPs, TiO_2 and gCN—can be used both individually and in combination for the chemical modification of textiles as a means to improve their functional properties. While two-component Ag/TiO_2 nanocomposites are already widely used for textile functionalisation, the application of Ag/gCN and TiO_2/gCN nanocomposites is relatively less researched [5]. Textile-based nanocomposites with incorporated Ag/gCN have been used in the development of triboelectric nanogenerators for wearable electronics and as environmentally friendly photocatalysts for organic reactions [32,33]. The latter include the oxidation of styrene to epoxide, ethylbenzene to acetophenone, and benzene to phenol, as well as the hydrogenation of 4-nitrophenol to 4-aminophenol [32]. TiO_2/gCN nanocomposite textiles have also been proven to be efficient photocatalysts for the degradation of environmental pollutants, including organic dyes such as methyl orange and Rhodamine B, the antibiotic sulfaquinoxaline, and the pesticide thiamethoxam [34–37]. In addition, these nanocomposites have been used in the production of antimicrobial textiles that exhibit a high antibacterial activity against *Escherichia coli* and *Staphylococcus aureus* [37].

The unique antimicrobial properties of Ag NPs, the excellent photocatalytic activity of TiO_2, and the ability of gCN to absorb visible light have attracted great research interest in the development of ternary Ag/TiO_2/gCN nanocomposites with enhanced photocatalytic and antimicrobial activity under solar light illumination. These nanocomposites have already been successfully used for the degradation of various pollutants, including acetaldehyde, phenol, and organic dyes, as well as for hydrogen production via water splitting, the photoreduction of Cr (VI) to Cr (III), and as antibacterial agents [38–42]. In the textile industry, Ag/TiO_2/gCN nanocomposites have been used for the photocatalytic degradation of dyes in textile wastewater. However, their direct application in the functionalisation of textile fibres is still unexplored and poses a challenge. The main challenges relate to the synthesis of Ag/TiO_2/gCN nanocomposites in the presence of textile fibres, especially due to the limitation of high calcination temperatures, which are not compatible with most textile materials. Furthermore, there are still significant opportunities for the development of sustainable approaches in the synthesis and application of Ag/TiO_2/gCN nanocomposites for the functionalisation of textiles.

This research aims to develop a novel nanotechnological process for the chemical modification of textile fibres via the ultrasound-assisted *in situ* sol–gel synthesis of Ag/TiO_2/gCN nanocomposites in the presence of a textile substrate that serves as a stabilising matrix. The approach involves the pre-synthesis of gCN, since its formation requires the thermal polycondensation of nitrogen-containing precursors at temperatures between 450 and 650 °C. These temperatures are unsuitable for *in situ* synthesis on cotton fibres, as they would lead to the thermal degradation of the cellulose macromolecule. Subsequently, TiO_2 and Ag NPs are synthesised *in situ* from appropriate precursors within the gCN suspension in the presence of a cotton substrate at temperatures that do not compromise the structural integrity of the fibres. This process facilitates the formation of a cotton-based matrix containing the Ag/TiO_2/gCN nanocomposite. We hypothesised that (i) despite the mild synthesis conditions, increasing the reaction temperature positively influences the morphological properties of the resulting nanocomposite, thereby enhancing its functionality and (ii) the presence of cotton during synthesis promotes the embedding of the Ag/TiO_2/gCN nanocomposite into the fibre structure, significantly affecting its distribution and overall loading. To validate these two hypotheses, the *in situ* synthesis of the Ag/TiO_2/gCN composite was performed at two increasing temperatures—20 and 70 °C. In addition, an *ex situ* approach was used in which the Ag/TiO_2/gCN nanocomposite was synthesised at 70 °C and was subsequently applied to cotton using the pad–dry–cure method. For comparative analysis, the two-component TiO_2/gCN nanocomposite and the one-component TiO_2 were also synthesised *in situ* under the same conditions. The functional properties of the chemically modified cotton were evaluated, focusing on the simultaneous photocatalytic self-cleaning, antimicrobial activity, and UV protection.

2. Experimental

2.1. Materials

A commercially bleached woven cotton (CO) fabric, with a mass per unit area of 120 g/m^2 and a density of 51 threads/cm in the warp and 31 threads/cm in the weft, was kindly provided for this study by Tekstina d. o.o., Ajdovščina, Slovenia. Titanium(IV) isopropoxide (TTIP; ≥97.8 % purity), $AgNO_3$ (≥99 % purity), acetic acid (99 % purity), L-ascorbic acid (L-AA; ≥99 % purity), isopropanol (IPA; ≥99 % concentration), p-benzoquinone, ethylenediaminetetraacetic acid disodium salt, and the organic dye Rhodamine B (RhB) were obtained from Sigma-Aldrich (USA). The layered particles of graphitic carbon nitride (gCN) were synthesised at the National Institute of Chemistry, Slovenia, in the Coatings Development Laboratory of the Department of Materials Chemistry. Two commercial TiO_2 products were used: anatase–rutile nano powder P25 (Evonik Industries AG, Germany) and dispersion with

5 nm crystals and a density of 1.2 g cm^{-3} (CCA200, Cinkarna, Kemična industrija Celje, d.d., Slovenia).

2.2. Chemical modification of CO samples

For the chemical modification of the CO samples, 1.0 mM $AgNO_3$, 3.0 % TTIP, and 0.5 % gCN were used. The *in situ* synthesis of Ag/TiO_2/gCN on the CO samples at 70 °C was carried out as follows (Fig. 1): First, 2 g gCN was dispersed in 98 g IPA in a beaker and was sonicated for 2 h. Then, a solution containing 12 g TTIP, 20 g acetic acid, and 68 g IPA was added. The beaker was placed on a magnetic stirrer to ensure the continuous mixing of the dispersion. Subsequently, the CO samples were immersed in the dispersion. Next, 0.068 g of $AgNO_3$ dissolved in 100 g of distilled water was added, followed by the dropwise addition of 100 g of a 12 mM aqueous solution of L-AA in order to reduce $AgNO_3$. The dispersion was additionally sonicated at 70 °C for 2 h to complete the synthesis. The use of IPA as the primary solvent was dictated by the solubility of TTIP, which readily dissolves and hydrolyses controllably in alcohol-based media. The subsequent addition of aqueous $AgNO_3$ and L-AA solutions to the basic IPA sol was a deliberate step aimed to provide the necessary ionic mobility for Ag^+ reduction while the mixed aqueous–IPA medium moderated nucleation, ensuring uniform Ag deposition. Furthermore, the presence of water was crucial to swell the cellulose substrate used during the synthesis, enabling deeper penetration of precursor species and promoting uniform coating of the Ag/TiO_2/gCN composite. The partial hydrolysis and surface hydroxylation of Ti species in this mixed medium also enhance interfacial adhesion between the inorganic and cellulose components, enabling interfacial bonding within the cellulose-based composite structure.

After synthesis, the CO samples were removed from the dispersion, squeezed with a two-roll padder to achieve a wet pickup of 95 ± 2 %, air-dried, cured at 150 °C for 5 min, rinsed three times with distilled water, and finally air-dried again. For comparison, TiO_2/gCN and TiO_2 were also synthesised *in situ* under the same conditions. To investigate the influence of the synthesis temperature on the functional properties of the chemically modified CO, the *in situ* syntheses of Ag/TiO_2/gCN, TiO_2/gCN, and TiO_2 at 20 °C were also performed. To evaluate the effect of the synthesis route, Ag/TiO_2/gCN, TiO_2/gCN, and TiO_2 were also synthesised *ex situ* at 70 °C i.e., in the absence of the CO substrate, in addition to the corresponding *in situ* preparation. These dispersions were applied to the CO samples using a pad–dry–cure process, which included immersing the CO samples into the dispersions for 1 min at 20 °C, squeezing with a wet pickup of 95 ± 2 %, air-drying, and curing at 150 °C for 5 min. Under the same conditions, 3 % of P25 and CCA200 were also applied to the CO samples, enabling a direct comparative analysis.

The synthesis temperatures of 70 °C and 20 °C were selected based on preliminary experiments. The higher temperature (70 °C) was reached intrinsically during sonication without additional heating and, together with the sonication process, was expected to provide sufficient activation energy for the chemical attachment of TiO_2 and the binary and ternary composites onto the cellulose backbone. To assess the influence of the synthesis temperature on the composite performance, 20 °C was also investigated for comparison.

Depending on the method of chemical modification, the CO samples were coded as listed in Table 1. After the removal of the CO samples, the remaining dispersions were centrifuged to separate the Ag/TiO_2/gCN, TiO_2/gCN, and TiO_2 powders, which were then air-dried. The powder samples were coded in the same way as the CO samples, but without the CO label.

Table 1
The sample codes and description of the chemical modification process of CO.

Sample code	Process description
CO(UN)	Untreated CO
CO(TiO_2)in70	Chemical modification of CO with TiO_2 by *in situ* synthesis at 70 °C
CO(TiO_2/gCN)in70	Chemical modification of CO with TiO_2/gCN by *in situ* synthesis at 70 °C
CO(Ag/TiO_2/gCN) in70	Chemical modification of CO with Ag/TiO_2/gCN by *in situ* synthesis at 70 °C
CO(TiO_2)in20	Chemical modification of CO with TiO_2 by *in situ* synthesis at 20 °C
CO(TiO_2/gCN)in20	Chemical modification of CO with TiO_2/gCN by *in situ* synthesis at 20 °C
CO(Ag/TiO_2/gCN) in20	Chemical modification of CO with Ag/TiO_2/gCN by *in situ* synthesis at 20 °C
CO(TiO_2)ex70	Chemical modification of CO with TiO_2 by *ex situ* synthesis at 70 °C
CO(TiO_2/gCN) ex70	Chemical modification of CO with TiO_2/gCN by *ex situ* synthesis at 70 °C
CO(Ag/TiO_2/gCN) ex70	Chemical modification of CO with Ag/TiO_2/gCN by *ex situ* synthesis at 70 °C
CO(TiO_2)P25	Chemical modification of CO with P25
CO(TiO_2)CCA200	Chemical modification of CO with CCA200

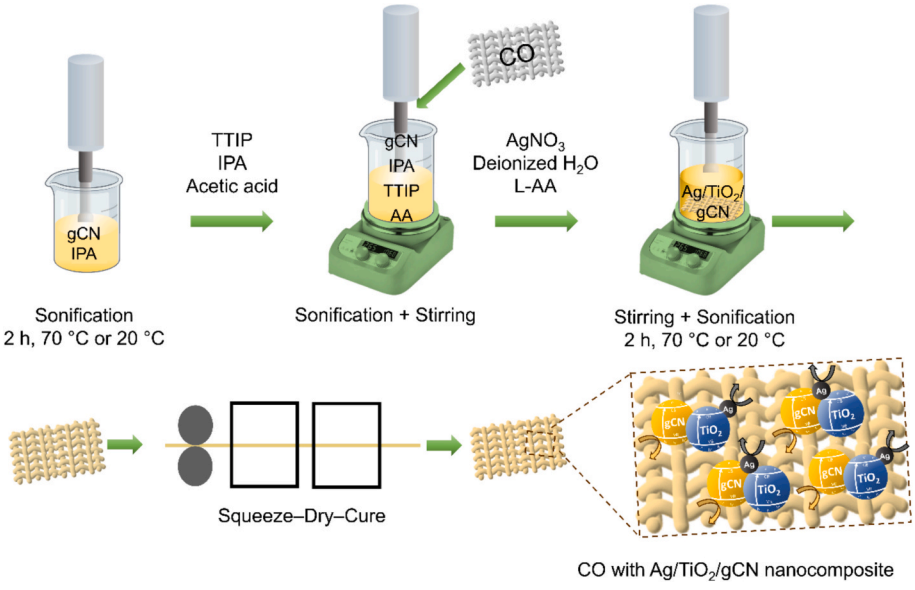

Fig. 1. The schematic representation of the *in situ* synthesis of Ag/TiO_2/gCN on the CO sample at 70 °C or 20 °C.

2.3. Structural characterisation

2.3.1. Scanning electron microscopy (SEM) and energy-dispersive spectroscopy (EDS)

The surface morphology of the CO samples was analysed using the SEM Zeiss Supra 35 VP (ZEISS, Germany), which was operated with a primary electron beam accelerated to 30 kV. The EDS spectra and the elemental mapping of C, Ti, Ag, O, and N were determined using the FEG SEM Thermo Fisher Quattro S electron microscope (Waltham, MA, USA) equipped with an Oxford Instruments Ultim® Max EDXS SDD detector (Abingdon, UK). Prior to both investigations, all samples were coated with a thin layer of carbon to provide conductivity and to improve the quality of the images.

2.3.2. Thin-layer wicking (TLW)

The surface free energy of the CO(UN) sample was determined from the thin-layer wicking measurement in the horizontal direction (TLW-H), which was described in detail in the Supplementary Material (Section S1) [43,44].

2.3.3. Nuclear magnetic resonance spectroscopy (NMR)

The NMR spectra of gCN sample were recorded on a 600 MHz Bruker spectrometer equipped with a 3.2 mm HX CPMAS iProbe. The Larmor frequencies for ^{1}H, ^{13}C, and ^{15}N nuclei were 600.23 MHz, 150.93 MHz, and 60.82 MHz, respectively. All measurements were performed under magic angle spinning (MAS) at 20 kHz. For the ^{1}H MAS NMR experiments, a 2.3 μs 90° pulse was followed by a 4.6 μs 180° echo pulse. A total of 64 scans were collected with a recycle delay of 3 s between scans. For the ^{13}C and ^{15}N NMR experiments, cross-polarization (CP) from ^{1}H nuclei was employed to enhance signal intensity. A 2.3 μs excitation pulse was first applied to the ^{1}H nuclei, followed by a CP block of 3.6 ms for ^{13}C and 3.0 ms for ^{15}N. During acquisition, high-power ^{1}H decoupling was applied to improve spectral resolution. The recycle delay was set to 3 s for both experiments. A total of 5120 scans were collected for the ^{13}C CPMAS spectrum and 20,480 scans for the ^{15}N CPMAS spectrum. The chemical shifts were referenced relative to tetramethylsilane (TMS (aq)) for ^{1}H and ^{13}C, and to liquid nitromethane (CH_3NO_2(aq)) for ^{15}N.

2.3.4. Inductively coupled plasma mass spectrometry (ICP-MS)

The concentrations of Ti and Ag on the CO samples were analysed via ICP-MS using a Perkin Elmer SCIED Elan DRC spectrophotometer. For each analysis, a sample of 0.5 g was prepared via acid decomposition using 65 % HNO_3 and 30 % H_2O_2 in a Milestone microwave system. The concentration of Ti and Ag were given as average values of the two independent measurements per sample, together with their standard deviation.

In addition, an ICP-MS analysis was performed to investigate the Ag release behaviour of the CO(Ag/TiO_2/gCN) sample. For this purpose, 1 g of each sample was immersed in 10 mL of a destined water and placed in a shaker at 25 °C for 3 and 15 h. After the indicated immersion times, the samples were blotted between two filter papers to remove excess liquid and then air-dried. The amount of Ag released from the sample was determined as the difference in Ag concentration (two independent measurements) on the sample before and after the experiment and expressed in percentage, together with their standard deviation.

2.3.5. X-ray photoelectron spectroscopy (XPS) and ultraviolet photoelectron spectroscopy (UPS)

The chemical composition of the surface and the type of chemical bonds in the CO samples were determined using the XPS PHI Genesis spectrometer from ULVAC-PHI Inc (Minnesota, USA) with a monochromatic Al source (photon energy 1486.68 eV). The analysed area had a diameter of 0.1 mm, while the depth of analysis was 2–5 nm. The high-energy XPS spectra were recorded with a pass energy of 27 eV for Ti, O, and C, as well as of 55 eV for Ag and N. Each sample was analysed in at least two places to check reproducibility. The XPS data were analysed using the XPS database and Multipak software version 9.9.

The UPS measurements were carried out with the same spectrometer using the He I (21.22 eV) discharge lamp. Before measurements, the samples were dried under vacuum and gently cleaned to remove weakly physiosorbed contaminants. To shifts low-energy electrons into the measurable kinetic-energy range, a negative bias of –10 V was applied. All spectra were processed using the manufacturer-provided analysis software.

2.3.6. Attenuated total reflection integrated Fourier transform infrared (ATR-FTIR) spectroscopy

The ATR-FTIR spectra were obtained using a Spectrum 3 FT-IR spectrometer (PerkinElmer, Inc., USA) equipped with an ATR diamond crystal cell with a refractive index of 2.0. The spectra were obtained throughout the frequency range of 4000–500 cm^{-1}, with a precision of 4 cm^{-1} and an average of 16 spectra per sample.

2.3.7. X-ray diffraction (XRD)

The crystalline structure of the powder and CO samples was studied with XRD using a PANalyticalX'Pert PRO X-ray diffractometer (XRD) ($CuK_{\alpha 1}$ = 1.5406 Å) with a fully open X'Celerator detector (2.1225°2θ). The XRD pattern was obtained by measuring the 2θ angle from 10 to 70 degrees, with a step size of 0.034 degrees and an integration duration of 100 s.

2.3.8. Nitrogen sorption analysis

The specific surface area, pore volume, and pore size of the powder samples were determined through nitrogen adsorption–desorption measurements at 77 K using a 3P Sync 220A device (3P, Odelzhausen, Germany). Before analysis, the samples were degassed for 2 h at 120 °C under vacuum. The specific surface area was determined using the Brunauer–Emmett–Teller (BET) method, while the pore size was determined using the Barrett–Joyner–Halenda (BJH) method.

2.3.9. UV–Vis spectroscopy

The transmission spectra of the CO samples were measured in the wavelength, λ, range of 200–800 nm using a Lambda 800+ UV/Vis spectrophotometer (Perkin Elmer, UK). At least thirteen measurements were taken for each sample, and the average transmittance, T, at each λ was calculated. The average transmission spectra were then transformed into absorption spectra using the following equation:

$$A = -\log T \tag{1}$$

where A denotes absorbance.

The optical band gap energies, E_g, of the chemically modified CO samples were determined from the absorption spectra using the Tauc relation [45], as follows:

$$(\alpha h\nu)^2 = K(h\nu - E_g) \tag{2}$$

where α represents the energy-dependent absorption coefficient (which is 2.303 × A), h is Planck's constant, ν is the radiation frequency, and K is a constant. According to Planck's radiation law, the energy, E, of the radiation is given as follows:

$$E = h\nu = \frac{1240}{\lambda} \tag{3}$$

The values of E_g are obtained by extrapolation to $\alpha = 0$ [45].

2.3.10. Photoluminescence (PL) spectra

The steady-state and dynamic PL measurements of the CO(TiO_2) in70, CO(TiO_2/gCN)in70, and CO(Ag/TiO_2/gCN)in70 samples were carried out with a modular spectrofluorometer (Horiba, model Fluorolog-QM 75–22) equipped with double excitation and emission monochromators. A CW 75 W xenon lamp and a 920 PMT detector (Horiba) cooled to −20 °C were used for the steady-state PL

measurements. The samples were loaded into a holder for solid samples and were measured at an angle of 35° to the incident beam. The excitation wavelength was set to 300 nm. The emission spectra were recorded in the wavelength range of 320–580 nm, with the excitation and emission slits set to 3.5 nm, respectively. A picosecond photon detector (Horiba, model PPD 850) was used for the time-correlated single photon counting (TCSPC) measurements. These measurements were performed with a nanosecond pulsed DeltaDiode LED light source with a nominal excitation wavelength of 285 and 325 nm, respectively. The width of the emission slits was set to 8 nm, and the response was measured at 446 nm (or 360 nm). The time window was set to 200 ns, with 4096 channels. A Ludox SM-30 solution of colloidal silica was used as a reference to determine the instrument response function (IRF), which was used to calculate the lifetimes of the charge carriers with the FelixFL spectroscopy software. The PL decay curves were fitted with a three-exponential function and deconvoluted with the instrument response function. The average lifetimes were calculated using Eqs. (S3)–(S7) (Section S2, Supplementary Material)). The fluorescence decay model was deconvoluted using the exponential model function in Eq. (S8) (Section S2, Supplementary Material)). Additionally, TCSPC measurements were performed to investigate the plasmonic effects associated with localised surface plasmon resonance (LSPR) on the CO (Ag/TiO_2/gCN)in70 sample. The sample was excited at 495 nm, which corresponds to the plasmon resonance region, and the emission decays were recorded at different detection wavelengths.

2.4. Photocatalytic activity

The photocatalytic activity of the CO samples was assessed by evaluating the degradation of a 0.02 mM RhB solution under solar light irradiation using a Xenotest Alpha instrument equipped with a xenon arc lamp equipped with the window optical filter (radiation range: 300–800 nm). The illumination intensity in the test chamber was 1.28 W/m^2. The CO samples (0.8 cm × 4.1 cm; 0.49 g) were immersed in 3 ml of the RhB solution in cuvettes and kept in the dark for 30 min to achieve adsorption–desorption equilibrium. The samples were then irradiated for 180 min, and the absorbance was measured every 30 min at the maximum absorption wavelength (equal to 552.93 nm) using a Lambda 850+ UV/Vis spectrophotometer (Perkin Elmer, Great Britain). The dye concentration at each time interval was calculated using previously established calibration curves.

The photocatalytic degradation of the RhB dye was determined by calculating the concentration ratio of C_t to C_0, where C_t represents the dye concentration at a given time of irradiation and C_0 is the initial dye concentration after the adsorption–desorption equilibrium. The apparent rate constant, k_{app}, of the photocatalytic reaction was determined in order to evaluate the efficiency of the photocatalytic degradation of the dye, assuming a pseudo-first-order kinetic behaviour, as described by the following equation [46]:

$$\ln\frac{C_t}{C_0} = -k_{app}t \tag{4}$$

where t represents the time of illumination.

Scavenging experiments were carried out to investigate the mechanism of the photocatalytic action of the CO(TiO_2/gCN)in70 and CO(Ag/TiO_2/gCN)in70 samples. As scavengers, isopropanol (IPA), p-benzoquinone (BQ), and ethylenediaminetetraacetic acid disodium salt (EDTA-2Na) were used to scavenge hydroxyl radicals ($^{\bullet}OH$), superoxide radicals ($^{\bullet}O_2^-$), and holes (h^+), respectively. The photocatalytic dye degradation experiments were performed under identical conditions as have previously been described, with 100 mM IPA, 1 mM BQ and 10 mM EDT-1Na added to the aqueous RhB dye solution. The apparent colouration rate constant, k'_{app}, was calculated from the kinetic data obtained for each scavenger, enabling the determination of which reactive species are important for the decolourisation mechanism (IDM) in the chemically modified CO samples, as follows:

$$\mathrm{IDM} = \frac{(k_{app} - k'_{app})}{k_{app}} x100 \tag{5}$$

where k_{app} is the decolourisation rate constant determined in the absence of the scavenger and k'_{app} is the decolourisation constant determined in the presence of the scavenger.

The reusability of the CO samples was evaluated using a five-cycle recycling experiment performed in accordance with photocatalytic dye degradation. After each cycle, the CO samples were removed from the test solution, washed with distilled water, and air-dried in the dark before being reused.

2.5. UV protection properties

The UV protection factor, UPF, of the CO samples was evaluated following the guidelines of Standard EN 13758–1:2001. Transmission was calculated for the UVA range from 315 to 400 nm and the UVB range from 280 to 315 nm. The UPF was determined using the following equation (SIST EN 13758–1:2002):

$$\mathrm{UPF} = \frac{\sum_{290}^{400}\mathrm{E}(\lambda)x\varepsilon(\lambda)x\Delta(\lambda)}{\sum_{290}^{400}\mathrm{E}(\lambda)x\varepsilon(\lambda)x\mathrm{T}(\lambda)x\Delta(\lambda)} \tag{6}$$

where E(λ) refers to the solar spectral irradiance, $\varepsilon(\lambda)$ is the relative erythemal effectiveness, $\Delta(\lambda)$ represents the wavelength interval, and T (λ) is the spectral transmittance at the given λ.

The UPF values were then categorised according to the Australian/New Zealand Standard for Sun-Protective Clothing—Evaluation and Classification (AS/NZS 4399, 2020). UPF values of 15 were categorised as “minimum protection”, values of 30 were categorised into the “good protection” category, and values of 50 were categorised into the “excellent protection” category.

2.6. Antimicrobial activity

The antimicrobial activity of the CO samples was evaluated against the Gram-positive bacteria *Staphylococcus aureus* (*S. aureus*; ATCC 6538) and the Gram-negative bacteria *Escherichia coli* (*E.coli*; DSM 18039) using the modified absorption process according to ISO 20743:2021. The bacterial strains were inoculated onto Tryptic Soy Agar (TSA) plates and incubated at 37 ± 2 °C for 24 h prior to the experiment. After incubation, a bacterial suspension at a concentration of 1×10^5 to 3×10^5 CFU/mL was prepared. The test samples (0.40 ± 0.05 g) were individually transferred into sterile 300 mL vessels. At the 0 h timepoint, 1 mL of the bacterial suspension was added to each sample. Immediately afterwards, 20 mL of neutralisation solution with 3 g of sterile glass beads was added, and the mixture was stirred. At the 24 h timepoint, the same procedure was performed; however, samples were first incubated at 37 ± 2 °C for 24 h before the neutralisation solution was added. This was followed by serial dilution, solid media inoculation, and incubation at 37 ± 2 °C for 24 h. Antimicrobial activity was calculated using the following equation:

$$A = (\log_{10}C_t - \log_{10}C_0) - (\log_{10}T_t - \log_{10}T_0) = F - G \tag{7}$$

where A represents the antibacterial activity value; $\log_{10} C_t$ and $\log_{10} T_t$ represent the average common logarithm for the number of bacteria obtained after 24 h from control and antibacterial-treated test samples, respectively; $\log_{10} C_0$ and $\log_{10} T_0$ represent the average common logarithm for the number of bacteria obtained immediately after inoculation from control and antibacterial-treated test samples, respectively; F represents the growth value on the control fabric ($F = \log_{10} C_t - \log_{10} C_0$); and G represents the growth value of the antibacterial-treated sample ($G = \log_{10} T_t - \log_{10} T_0$).

2.7. Cytotoxicity evaluation

The cytotoxicity of the untreated CO sample and the CO modified with TiO_2/gCN and Ag/TiO_2/gCN nanocomposites synthesised via an *in situ* process at 70 °C was assessed following ISO 10993–5:2009, using the direct contact method. Standardised BALB/3T3 clone A31 mouse fibroblasts (ATCC® CCL-163™) were used as the standardised cell lines on which the samples were directly placed. The cultures were incubated for 24 h at 37 ± 1 °C in 5 ± 1 % CO_2. After incubation, cells were examined microscopically for morphological changes, and cell viability was determined using the Neutral Red uptake assay. Absorbance at 540 nm was measured with a microplate reader (Gen5™, BioTek). Controls (positive = non-cytotoxic; negative = cytotoxic) were included.

Cell viability was calculated according to the following formula:

$$\text{Viability} = \frac{A_{\text{sample}} - A_{\text{blank}}}{A_{\text{negative control}} - A_{\text{blank}}} (\%) \quad (8)$$

where A_{sample} represents the absorbance of the test sample, A_{blank} represents the absorbance of the medium (no cells), and $A_{\text{negative control}}$ represents the absorbance of the negative control.

3. Results and discussion

3.1. Surface morphology and chemical composition

The surface morphology of the CO(UN), CO(Ag/TiO_2/gCN)in70, CO(Ag/TiO_2/gCN)in20, and CO(Ag/TiO_2/gCN)ex70 samples was examined using SEM (Fig. 2(a-d)). SEM micrographs revealed that the chemical modification of the CO samples with Ag/TiO_2/gCN nanocomposites resulted in the increased surface roughness of the cellulose fibres compared to the untreated CO(UN) sample, regardless of the nanocomposite synthesis method. As anticipated, the CO(Ag/TiO_2/gCN)ex70 sample, for which the nanocomposite was synthesised *ex situ* and subsequently applied to the CO samples via the pad–dry–cure process, exhibited the least pronounced morphological alterations. In contrast, the ultrasound-assisted *in situ* synthesis of Ag/TiO_2/gCN nanocomposites in the presence of the CO substrates at both 70 °C and 20 °C led to the formation of a higher density of surface protrusions and fibre entanglements, indicating more significant morphological modifications. The EDS spectrum (Fig. 2(e)) and elemental mapping (Fig. 2(f)) of the CO(Ag/TiO_2/gCN)in70 sample confirmed the presence of C, O, Ti, N, and Ag. While the C and O signals were attributed to cellulose, gCN, and TiO_2, the detection of Ti, N, and Ag signals provided direct evidence for

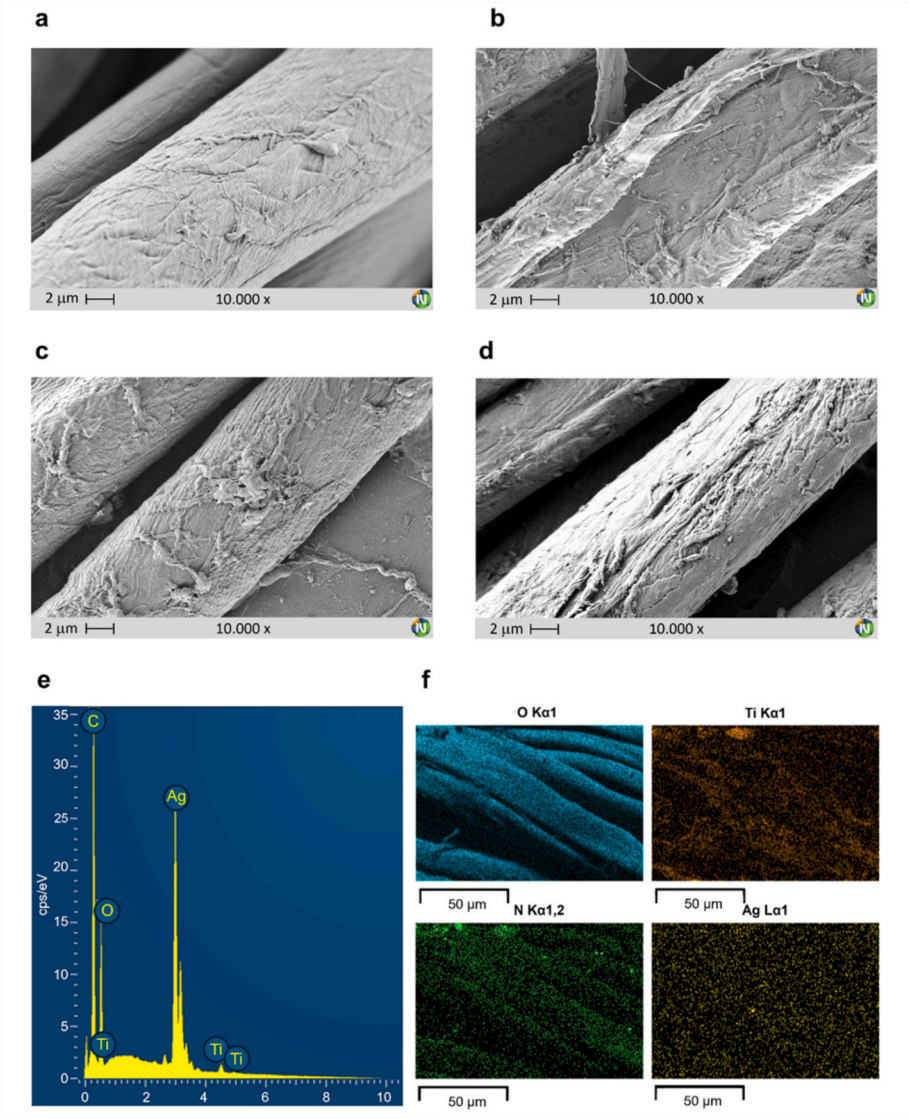

Fig. 2. SEM images of untreated CO(UN) (a) and chemically modified CO(Ag/TiO_2/gCN)in70 (b), CO(Ag/TiO_2/gCN)in20 (c), and CO(Ag/TiO_2/gCN)ex70 (d) samples; EDS spectra (e) and element mapping images (f) of the CO(Ag/TiO_2/gCN)in70 sample.

the successful incorporation of Ag/TiO_2/gCN nanocomposites. Moreover, elemental mapping revealed the relatively uniform distribution of these nanocomposites across the fibre surface.

Since nanocomposite adhesion and distribution on the CO samples are predominantly governed by surface and interfacial forces, a quantitative evaluation of the surface free energy of the CO(UN) sample was conducted to elucidate the energetic parameters controlling nanoparticle immobilisation [43,44]. The total surface free energy (γ_S^{tot}) of CO (UN) was determined to be 55.9 mJ/m^2, dominated by an exceptionally high electron-donor component (γ_S^- = 55.4 mJ/m^2) (Section S1, Table S2, Supplementary Material), reflecting the polar and hydrophilic nature of the cellulose fibres. The strong γ_S^- contribution is consistent with the abundance of surface hydroxyl groups along the cellulose backbone, which confer significant hydrogen-bonding capability and favour acid-base interactions with the TiO_2, TiO_2/gCN, and Ag/TiO_2/gCN coatings that contain hydroxylated and/or oxide functionalities. These surface characteristics promote robust interfacial adhesion through the combined action of Lifshitz–van der Waals, electrostatic, and Lewis acid–base interactions. This interpretation is further supported by the calculated work of adhesion (W_a) between cellulose fibres and water, which is equal to 81.7 mJ/m^2 (Section S1, Table S3, Supplementary Material). This value lies within the high-adhesion regime, consistent with strong interactions at the cellulose/water interface. Furthermore, literature reports indicate that the presence of metal oxides in the contacting liquid phase reduces the interfacial tension at the solid–liquid boundary [47], thereby increasing the effective work of adhesion and strengthening nanoparticle immobilisation.

The chemical structure of the gCN sample was further characterised using solid-state NMR spectroscopy (Fig. 3). The ^{15}N cross-polarization magic-angle spinning (CPMAS) NMR spectrum revealed four distinct signals corresponding to different nitrogen environments within the gCN structure, confirming the presence of the hydrogen-bonded melon structure. Specifically, the peak at −191 ppm is assigned to outer nitrogen species, while the signal at −226 ppm corresponds to inner nitrogen species and appears weaker due to their greater distance from protons. The peaks at −246 ppm and −265 ppm are attributed to NH and NH_2 groups, respectively, consistent with ab initio calculations [48]. In ^{13}C CPMAS spectrum, two main signals at 155 and 164 ppm correspond to the inner and outer carbon species. The broad signal at 164 ppm, along with noticeable shoulders, suggests the presence of multiple chemical environments, such as protonated, deprotonated, surrounded, or partially polymerised gCN structures. The ^1H MAS NMR can reveal the protons in aliphatic groups, residual water, NH_x groups, and hydrogen bonds. The broad resonance at ~8.8 ppm is assigned to hydrogen-bonded amino groups, whereas the signals at ~3–5 ppm can be attributed to non-hydrogen-bonded NH_x species and residual water [49–51].

The concentrations of TiO_2 and Ag NPs deposited on the chemically modified CO samples were quantified using ICP-MS and are summarised in Table 2. The results reveal that despite the use of constant concentrations of TTIP and $AgNO_3$ precursors in the synthesis processes, the final loading of TiO_2 and Ag NPs was significantly influenced by the chemical modification method. In particular, the highest concentrations of TiO_2 were observed in CO samples chemically modified by the *in situ* synthesis of TiO_2, TiO_2/gCN, and Ag/TiO_2/gCN at 70 °C. These values were markedly higher than those obtained by both *ex situ* synthesis at 70 °C and *in situ* synthesis at 20 °C, suggesting that both the synthesis temperature and the synthesis route play a crucial role in TiO_2 deposition efficiency. A similar trend was observed for Ag NPs, whereby the Ag NPs content in the CO(Ag/TiO_2/gCN)in70 sample was twice that of the CO(Ag/TiO_2/gCN)in20 sample and more than 3.6 times higher than in the CO(Ag/TiO_2/gCN)ex70 sample. These results clearly demonstrate that the presence of the CO substrate during *in situ* synthesis at elevated temperatures significantly improves the deposition of both nanoparticles and nanocomposites.

Table 2
Concentrations of Ti and Ag in chemically modified CO samples determined using ICP-MS.

Sample	Ti (mg/kg)	Ag (mg/kg)
CO(TiO_2)in70	9986 ± 310	0
CO(TiO_2/gCN)in70	12047 ± 628	0
CO(Ag/TiO_2/gCN)in70	11952 ± 717	197 ± 8
CO(TiO_2)in20	4866 ± 93	0
CO(TiO_2/gCN)in20	5739 ± 328	0
CO(Ag/TiO_2/gCN)in20	4798 ± 256	98 ± 5
CO(TiO_2)ex70	7126 ± 520	0
CO(TiO_2/gCN)ex70	5789 ± 372	0
CO(Ag/TiO_2/gCN)ex70	5109 ± 249	55 ± 2

A comprehensive analysis of the surface elemental composition and the chemical bonding of the CO samples was conducted using XPS analysis with the corresponding data being summarised in Table S4 (Section S3, Supplementary Material). The survey XPS spectra revealed prominent peaks corresponding to the carbon (C 1s) and oxygen (O 1s) of the cellulose in all CO samples. The chemical modification of the CO samples led to a reduction in the relative carbon content, which can be attributed to the surface coverage of the cellulose matrix by the TiO_2, TiO_2/gCN or Ag/TiO_2/gCN components. At the same time, an increase in the oxygen content and O/C atomic ratio was observed in all modified samples, indicating the increased surface oxidation of the cellulose due to the introduction of TiO_2.

In addition to the C 1s and O 1s peaks, the chemically modified CO sample exhibited a Ti 2p peak, confirming the presence of titanium species. In addition, a N 1s peak was detected in the gCN-containing samples, as well as a Ag 3d peak in the Ag-containing, confirming the incorporation of nitrogen and Ag, respectively.

To determine the surface chemical states and the bonding environments, the high-energy-resolution XPS spectra of C 1s, O 1s, Ti 2p, N 1s, and Ag 3d were recorded and deconvoluted into individual components according to the specific functional groups and bond types. These detailed spectral fits are shown in Fig. 4 and Figs. S2–S10 (Section S3,

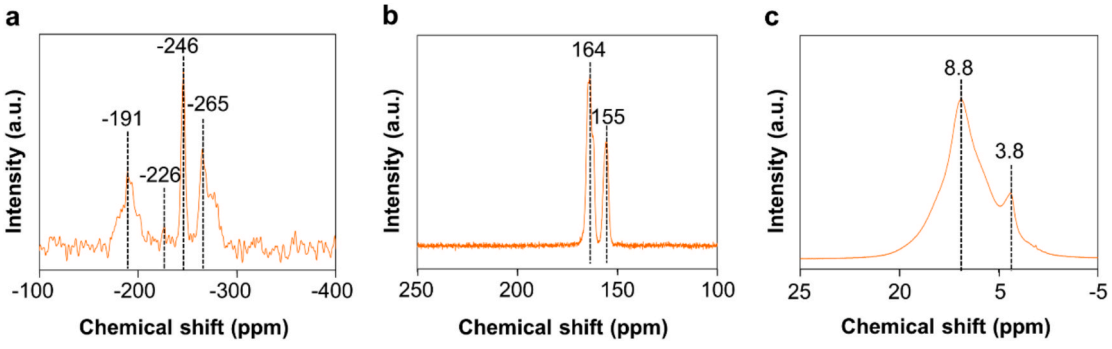

Fig. 3. ^{15}N CPMAS (a), ^{13}C CP MAS (b), and ^1H MAS (c) NMR spectra of gCN powder.

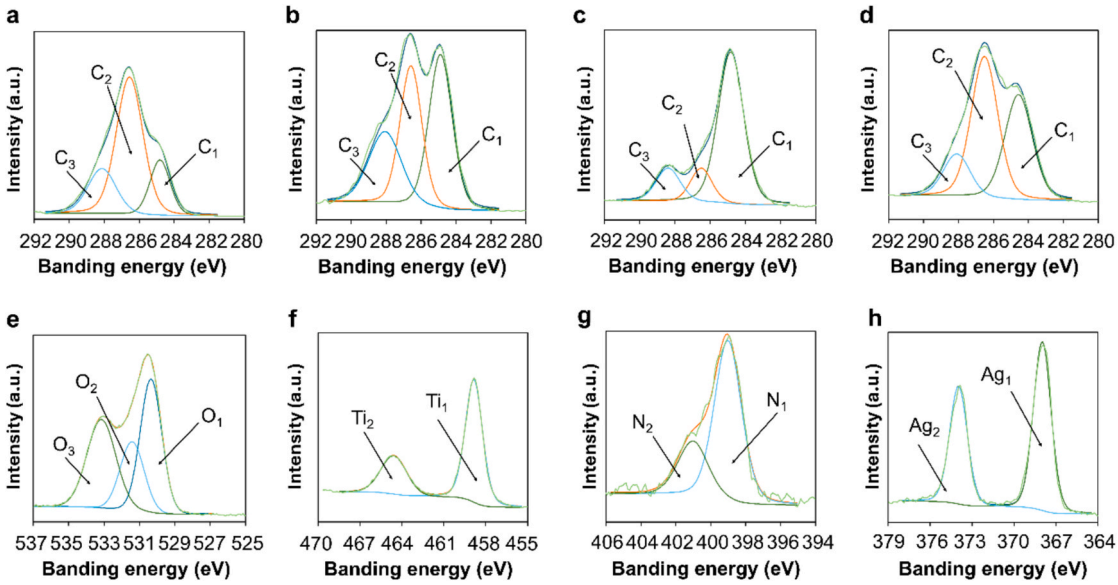

Fig. 4. The deconvolution of the high-resolution XPS C 1s spectra for CO(UN) (a), CO(Ag/TiO_2/gCN)in70 (b), CO(Ag/TiO_2/gCN)in20 (c), and CO(Ag/TiO_2/gCN)ex70 (d) samples, as well as O 1s (e), Ti 2p (f), N 1s (g), and Ag 3d (h) spectra of the CO(Ag/TiO_2/gCN)in70 sample.

Supplementary Material).

The deconvolution of the C 1s spectra of the CO(UN), CO(Ag/TiO_2/gCN)in70, CO(Ag/TiO_2/gCN)in20, and CO(Ag/TiO_2/gCN)ex70 samples revealed three distinct peaks that were characteristic for cellulose-derived carbon species (Fig. 4(a–d)). The peak denoted as C_1 at 285.0 eV is attributed to C–C/C–H bonds, the C_2 peak at 286.5 eV corresponds to C–O/C–OH/C–N bonds and the C_3 peak at 287.5 eV is assigned to O–C–O bonds [52–54]. After the chemical modification of the CO samples, an increase in the relative area of the C_1 peak was observed, along with a simultaneous decrease in the relative area of the C_2 peak. These variations indicate changes in the chemical composition of the surface due to the partial masking or transformation of the cellulose functional groups during the introduction of the TiO_2, gCN, and Ag NPs species.

The deconvolution of the O 1s spectra of the CO(UN) sample (Fig. S2) exhibits a dominant O_2 peak at 532.8 eV, which is typical of an organic oxide environment, including C–O in polysaccharides and –OH of the adsorbed water. In contrast, chemically modified CO samples revealed three different peaks (Fig. 4(e)). The strong O_1 peak at ~530 eV is assigned to lattice oxygen in Ti–O bonds, thereby confirming the successful incorporation of TiO_2. The O_2 and O_3 peaks, located at 531–532 eV and at 533–534 eV, respectively, are associated with the hydroxyl groups (–OH), ether or alcohol functionalities (C–O), and carbonyl species (C═O) present in the cellulose matrix [55].

The presence of TiO_2 in the chemically modified CO samples was further confirmed by the Ti 2p spectra, which exhibited two characteristic peaks—Ti_1 at ~458.5 eV (Ti $2p_{3/2}$) and Ti_2 at ~464.3 eV (Ti $2p_{1/2}$)—indicating the Ti^{4+} valence state in the anatase phase of TiO_2 (Fig. 4(f)) [55,56].

Two peaks were identified in the N 1s spectra of the gCN-containing samples—N_1 at 399.0 eV, which corresponds to the amine or amide nitrogen (N–H), as well as the N_2 peak at 400.7 eV, which is attributed to graphitic nitrogen species such as C–N═C, $–NH_2$, or ═NH moieties—indicating the gCN framework (Fig. 4(g)) [57,58].

The Ag 3d spectra of the CO(Ag/TiO_2/gCN)in70 and CO(Ag/TiO_2/gCN)in20 samples exhibited two peaks—Ag_1 at 367.0 eV (Ag $3d_{5/2}$) and Ag_2 at 373.8 eV (Ag $3d_{3/2}$)—confirming the presence of Ag NPs in the composite structures (Fig. 4(h)) [55].

A detailed deconvolution of the C 1s and O 1s spectra of the untreated and chemically modified CO samples provides insight into chemical interactions between TiO_2 and the cellulose backbone, particularly the formation of C–O–Ti bonds. Although the C–O–Ti signal in the C 1s spectra is partially obscured within the shoulder of the main C 1s peaks, the analysis of CO(UN) and CO(Ag/TiO_2/gCN) (Fig. 4(b,c,d)) reveals significant changes in the relative intensities of the C_1, C_2 and C_3 components, suggesting the formation of additional interfacial bonding during *in situ* synthesis at 70 °C (Table S1). Complementing this, the O 1s spectrum of CO(Ag/TiO_2/gCN) (Fig. 4e) exhibits a pronounced intermediate O_2 component at 532.1 eV, which lies between the contributions of organic oxygen (O_3) and TiO_2 lattice oxygen (O_1). This is consistent with oxygen species at the interface bridging carbon and titanium to form C–O–Ti bonds. Overall, these results demonstrate that the interactions between TiO_2 and cellulose cannot be ascribed solely to physisorption and that the sonication-assisted *in situ* sol–gel synthesis, particularly at elevated temperatures, promotes chemical coupling at the organic–inorganic interface and enables the formation of stable heterostructure composites.

To confirm the formation of stable heterostructure composites through C–O–Ti bonding at the organic–inorganic interface, the FTIR spectroscopy was conducted for the CO(TiO_2)in70, CO(TiO_2/gCN)in70 and CO(Ag/TiO_2/gCN)in70 samples (Fig. 5). Comparative analysis of the spectra (Fig. 5a) demonstrated distinct chemical changes within the cellulose matrix following the *in situ* synthesis of TiO_2, TiO_2/gCN, and Ag/TiO_2/gCN conducted at 70 °C. Compared to untreated cotton, treated samples exhibited broadening and increased intensity of the O–H stretching band (3600–3200 cm^{-1}) and the H–O–H bending vibration near 1636 cm^{-1}, indicating formation of surface Ti–OH groups and enhanced water adsorption on TiO_2. Additional absorption bands at 1500–1650 cm^{-1} (A in Fig. 5a) as well as at 835–805 cm^{-1} (E in Fig. 5a) spectral regions of the CO(TiO_2/gCN)in70 and CO(Ag/TiO_2/gCN)in70 samples correspond to aromatic C–N stretching and out-of plane bending vibration of triazine units of gCN [41,59], confirming its incorporation within the cellulose matrix. Successful coupling of TiO_2/gCN heterostructure with cellulose can be further supported by the increase of the intensities of the absorption bands in the 1427–1406 cm^{-1} (B in Fig. 5a) spectral region, attributed to CH_2 scissoring (δCH_2) vibration of cellulose backbone. Since these bands are sensitive to hydrogen bonding and crystalline ordering [60,61], their enhancement implies the establishment of chemical and/or hydrogen-bonding interactions between the cellulose matrix and TiO_2/gCN. The most prominent changes occurred in the 1200–900 cm^{-1} (C and D in Fig. 5a) cellulose fingerprint region, where a new shoulder appeared at ~ 1014 cm^{-1} accompanied by

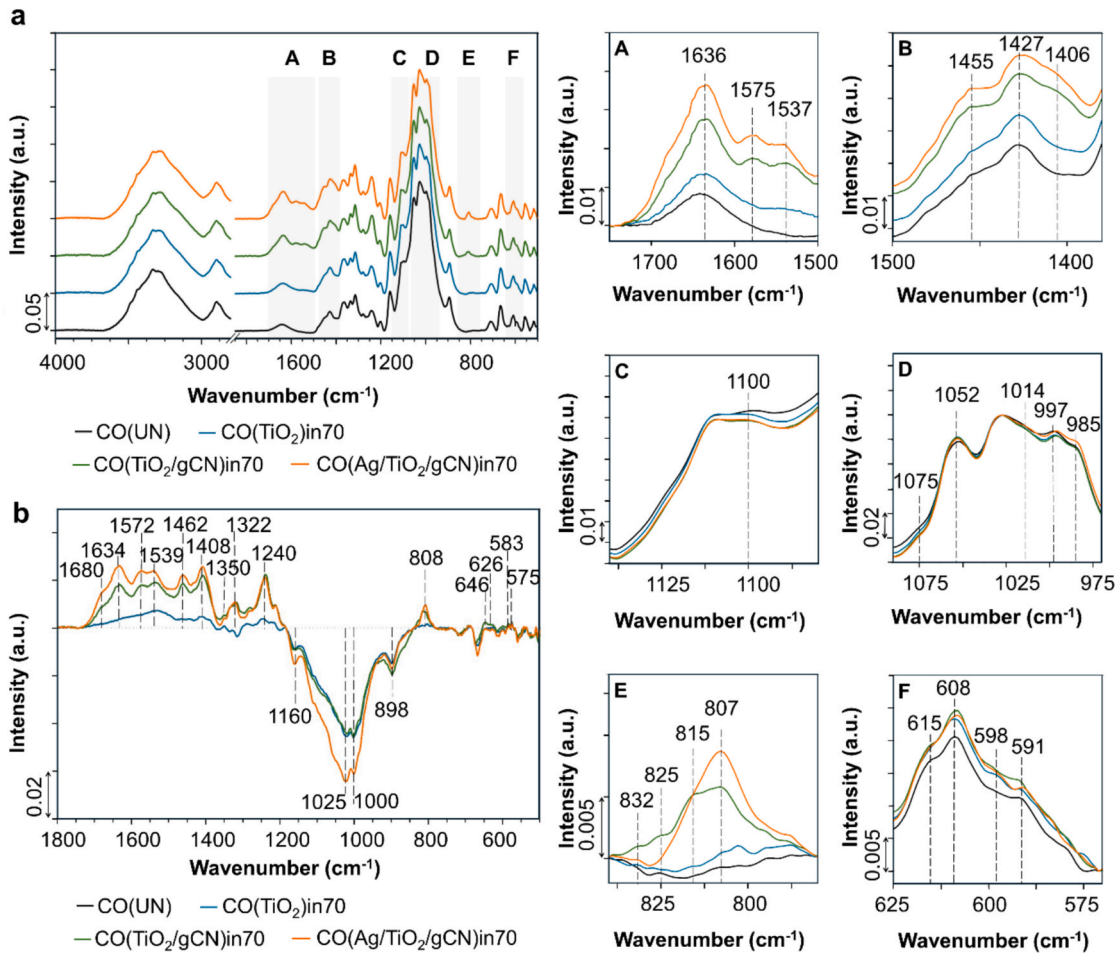

Fig. 5. ATR-FTIR spectra of the untreated CO and CO chemically modified with TiO_2, TiO_2/gCN and Ag/TiO_2/gCN prepared via in-situ synthesis at 70 °C (a) with marked and enlarged regions of interest (A–F), and differential spectra of the CO(TiO_2)in70, CO(TiO_2/gCN)in70 and CO(Ag/TiO_2/gCN)in70 samples obtained by using the ATR-IR spectrum of the CO(UN) sample as the background (b).

shifts and intensity variations of the bands near 1075–985 cm^{-1}. These changes can be attributed to the formation of interfacial Ti–O–C linkages between Ti species and cellulose hydroxyls and to perturbation of the glycosidic and C–O–C stretching modes of cellulose, supported by a slight decrease of the absorption band at 1100 cm^{-1}. The emergence of distinct Ti–O–Ti lattice vibrations at 620–580 cm^{-1} (F in Fig. 5a) further verified the formation of TiO_2 networks on the cellulose surface [59,60].

To obtain comprehensive insights into the interactions between TiO_2-based heterostructures and cellulose fibres, differential spectra were employed. Accordingly, the IR-ATR spectrum of untreated cotton (CO(UN)) was subtracted from those of TiO_2-, TiO_2/gCN-, and Ag/TiO_2/gCN-treated samples to highlight subtle changes induced by the *in situ* synthesis at 70 °C (Fig. 5b). The resulting differential spectra revealed distinct positive and negative bands, indicating both the consumption and formation of chemical functionalities upon nanoparticle anchoring. Negative peaks in the 1160–1020 cm^{-1} region correspond to the reduction of C–O and C–O–C stretching vibrations of cellulose [60,62], most likely due to the incorporation of TiO_2, gCN, and Ag species, which restrict the vibrations of cellulose macromolecules. In particular, the negative absorption bands at 1025 cm^{-1}, attributed to the stretching of secondary alcohol groups of cellulose, clearly indicate their participation in the formation of interfacial Ti–O–C linkages [63,64]. Positive bands appearing at 1680–1240 cm^{-1} and at 808 cm^{-1} are assigned to the presence of gCN, undoubtedly confirming its successful incorporation within the cellulose matrix. The enhanced intensity in the 650–600 cm^{-1} region corresponds to Ti–O–Ti lattice vibrations, consistent with the formation and stabilization of TiO_2 nanoparticles within the cellulose matrix (ref). These differential analyses demonstrate that *in situ* synthesis at 70 °C modified the cellulose backbone not only through hydrogen-bonded (Ti–OH···O–cellulose) interactions but also via covalent (Ti–O–C) bond formation, resulting in strong interfacial binding between the organic matrix and the TiO_2-based heterostructures. These FTIR results, along with the XPS-observed shifts in Ti 2p and O 1s binding energies, confirm the formation of chemical bonds between the inorganic coating and the cotton substrate. This covalent interfacial coupling explains the exceptional stability and recyclability of the *in situ* synthesised composites.

3.2. Crystal structure

The XRD patterns of the TiO_2, TiO_2/gCN, and Ag/TiO_2/gCN powder samples synthesised *in situ* at 70 °C and 20 °C, as well as those of the corresponding chemically modified and untreated CO samples, are presented in Fig. 6. In all powder samples (Fig. 6(a,b)), the characteristic diffraction peaks of TiO_2 at $2\theta = 25.97°$, 38.51°, 47.57°, 54.45°, and 62.19°, correspond to the (1 0 1), (0 0 4), (2 0 0), (2 1 1), and (2 0 4) planes of anatase TiO_2 (JCPDS No. 21-1272) were presented, irrespective of their composition or synthesis temperature and route [65,66]. These results confirm that the crystallisation of TiO_2 already takes place at relatively low synthesis temperatures. However, the broadened and less-intense diffraction peaks indicate incomplete crystallisation, suggesting that some of the TiO_2 remained in an amorphous or poorly crystalline state. In addition, two weak diffraction peaks at approximately $2\theta = 31°$ and 44° were observed in the (TiO_2)in70 and

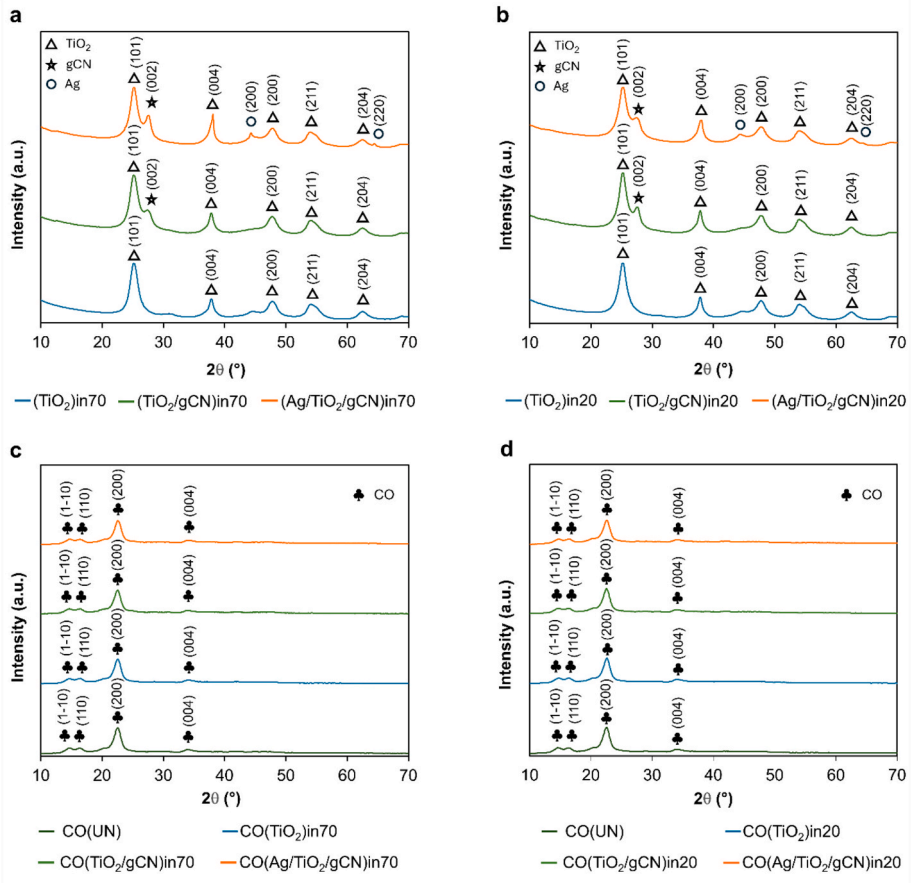

Fig. 6. The XRD patterns of the TiO_2, TiO_2/gCN, and Ag/TiO_2/gCN powder samples synthesised at 70 °C (a) and 20 °C (b), as well as the untreated CO sample and CO samples chemically modified with TiO_2, TiO_2/gCN, and Ag/TiO_2/gCN produced by *in situ* synthesis at 70 °C (c) and 20 °C (d).

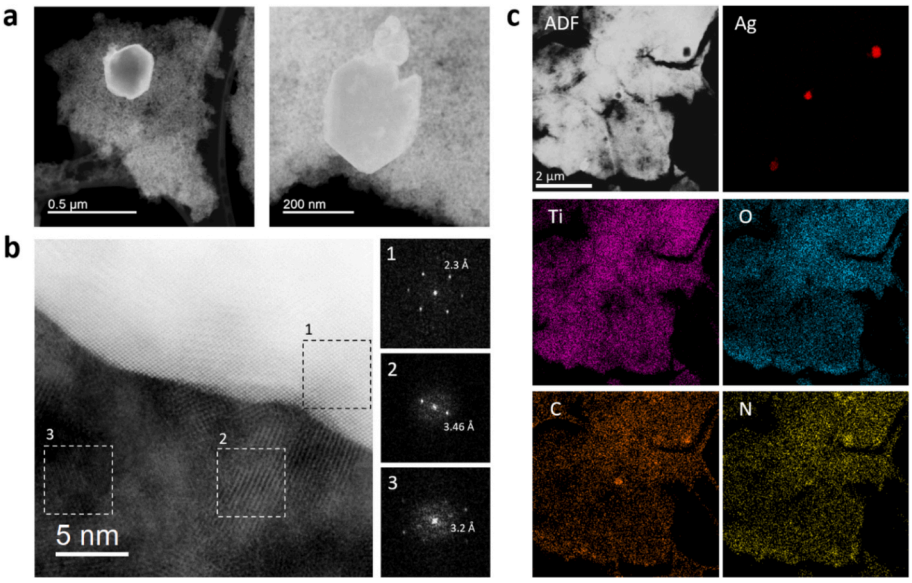

Fig. 7. ADF images of two different regions of the composite where Ag nanoparticles rest on TiO_2/gCN (a). A compose image of BF + ADF signals displaying the edge of an Ag nanoparticle and the support TiO_2/gCN (b). The Fast Fourier Transform series on the right side correspond to the regions marked by the dotted squares indicated by numbers. From each one of them the interplanar lattice distance can be measured corresponding to Ag in 1, TiO_2 in 2 and gCN in 3 (the value of the measured spots is displayed in Å for easier plane identification in the real space, although the FFT spacing corresponds to the reciprocal space 1/Å). ADF and EDS signals are shown in (c) for each element of the Ag/TiO_2/gCN nanocomposite.

(TiO_2)in20 powder samples, which are likely due to minor impurities.

For gCN, a strong diffraction peak at 2θ = 28.35° was clearly visible in the samples of the TiO_2/gCN and Ag/TiO_2/gCN nanocomposites synthesised at both 70 °C and 20 °C (Fig. 6(a,b), which corresponds to the (0 0 2) crystal planes of graphitic materials, indicating the typical interlayer stacking of the conjugated aromatic gCN systems (JCPDS No. 87-1526) [67,68]. For metallic Ag in the (Ag/TiO_2/gCN)in70 and (Ag/TiO_2/gCN)in20 powder samples, diffraction peaks at 44.3° and 64.7° were indexed to the (2 0 0) and (2 2 0) planes, respectively, consistent with the face-cantered cubic structure of Ag (JCPDS No. 04-0783) [69,70]. The clear identification of all peaks confirms the successful formation of the two- and three-component composites, thus demonstrate the coexistence of TiO_2, gCN and Ag in the composite structures.

The XRD patterns of the CO-based samples (Fig. 6(c,d)) revealed prominent diffraction peaks at 2θ = 14.86°, 16.12°, 22.69°, and 34.57, which can be assigned to the (1 –1 0), (1 1 0), (2 0 0), and (0 0 4) planes of crystalline cellulose I (JCPDS 03-0226), respectively [71,72]. Remarkably, no diffraction peaks corresponding to the TiO_2, gCN, and Ag NPs phases were detected in these patterns, most likely because they are overshadowed by the dominant diffraction peaks of cellulose.

The Ag/TiO_2/gCN nanocomposite was also analysed with STEM (Fig. 7). In Fig. 7(a) ADF images of the Ag nanoparticles resting on the TiO_2/gCN support reveal the typical size of around 300 nm, while the overall size of the nanoparticles ranged between 100 nm and 700 nm. The shape of the nanoparticles varied from round to irregular and in some cases exhibited a faceted morphology. An area where the lattice spacing is visible along the edge of an Ag nanoparticle together with the support TiO_2/gCN is shown in Fig. 7(b).

The interplanar lattice distances were estimated from the Fast Fourier Transform (FFT) patterns of the regions marked with dotted squares. In square 1, the distance of 2.3 Å corresponds to the (1 1 1) plane of face-centred cubic (FCC) Ag. In square 2, the distance of 3.46 Å corresponds to the (0 1 1) plane of anatase TiO_2. In square 3, the distance of 3.2 Å corresponds to the (0 0 2) plane of gCN. In addition, EDS maps were carried out to identify the element distribution in the Ag/TiO_2/gCN nanocomposite (Fig. 7(c)). The Ag signal matches very well to the

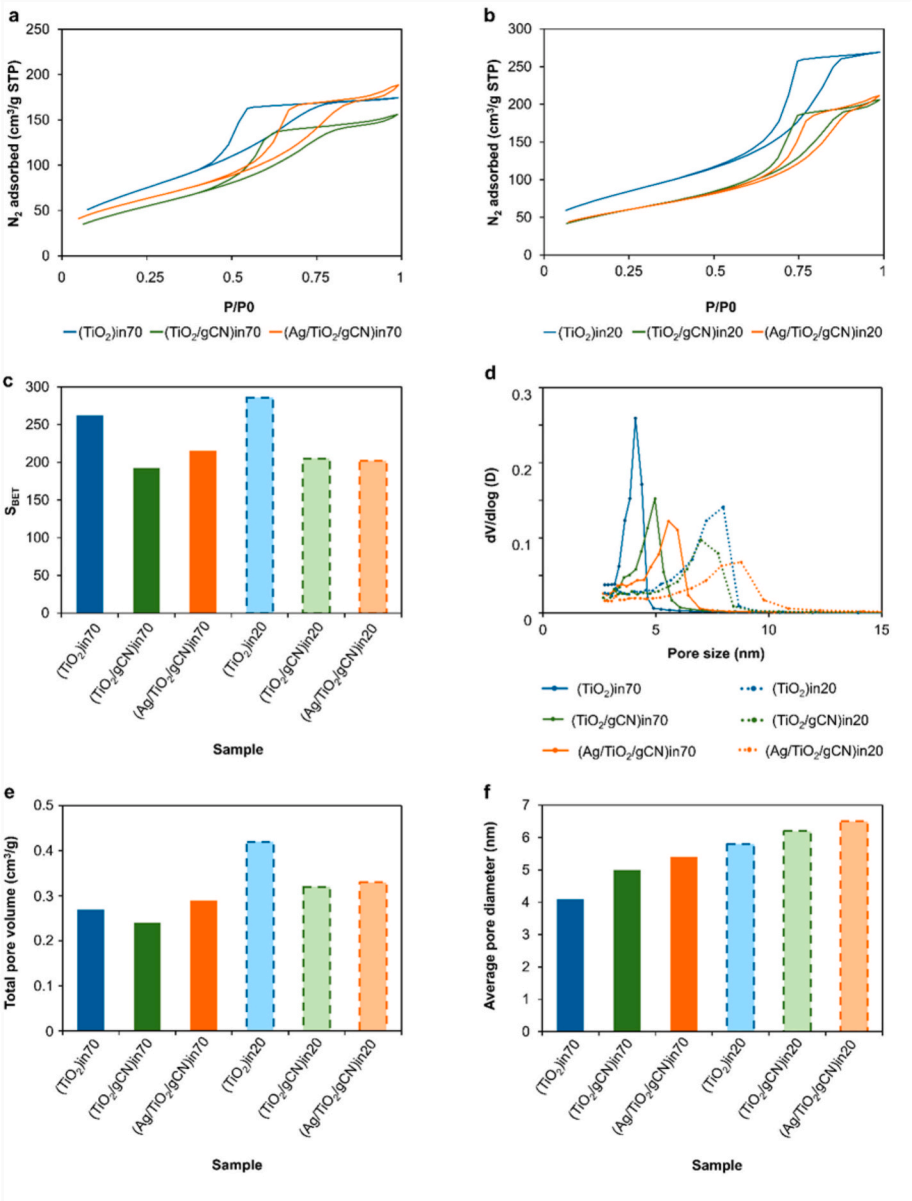

Fig. 8. The nitrogen adsorption–desorption isotherms (a,b), specific surface area, S_{BET}, based on BET theory (c), pore size distributions (d), total pore volume (e), and average pore diameter (f) of the TiO_2, TiO_2/gCN, and Ag/TiO_2/gCN powder samples synthesised *in situ* at 70 °C and 20 °C.

location of the particles appearing in the corresponding ADF image. In the case of Ti and O, the maps show an even distribution of the signal along the support. For C and N, the overall signal distribution seems to be homogeneous too, except for few spots that probably correspond to the formation of smaller patches.

3.3. Textural properties

The textural properties of the TiO_2, TiO_2/gCN, and Ag/TiO_2/gCN powder samples synthesised *in situ* at 70 °C and 20 °C were determined using the nitrogen adsorption–desorption isotherms (Fig. 8). All samples show type IV isotherms with H2 hysteresis loops according to the IUPAC classification, which is characteristic of mesoporous materials [73]. The results show that both the composition of the powder samples, as well as the synthesis temperature, influenced the specific surface area and pore structure (Fig. 8(c)). Accordingly, at the same synthesis temperature, the highest BET specific surface areas with the lowest pore size were obtained for the one-component (TiO_2)in70 and (TiO_2)in20 samples (Fig. 8 (c,d)).

The incorporation of gCN and Ag NPs resulted in a reduction in the specific surface area and an increase in the average pore diameter of the nanocomposites compared to the one–component (TiO_2)in70 and (TiO_2) in20 samples at both synthesis temperatures. This reduction in specific surface area with a simultaneous increase in pore size could be attributed to the partial blocking or filling of the smaller pores by the deposited gCN and Ag NPs within the nanocomposite structure.

At the same time, the samples synthesised at 70 °C exhibited a slightly lower pore volume and average pore diameter compared to the samples synthesised at 20 °C (Fig. 8(e,f)). This suggests that at 70 °C, the sol–gel network may undergo faster condensation and cross-linking reactions, leading to denser structures with smaller and fewer pores. Accordingly, the (TiO_2)in70 sample had the smallest pore diameter of 4.1 nm with the most uniform pore distribution, while the (Ag/TiO_2/gCN)in20 sample exhibited the largest average pore diameter of 6.5 nm with the broadest pore distribution ranging from 3 nm to 14 nm.

3.4. Optical absorption properties

The optical absorption properties of the untreated and chemically modified CO samples were analysed using UV–Vis spectroscopy, and the

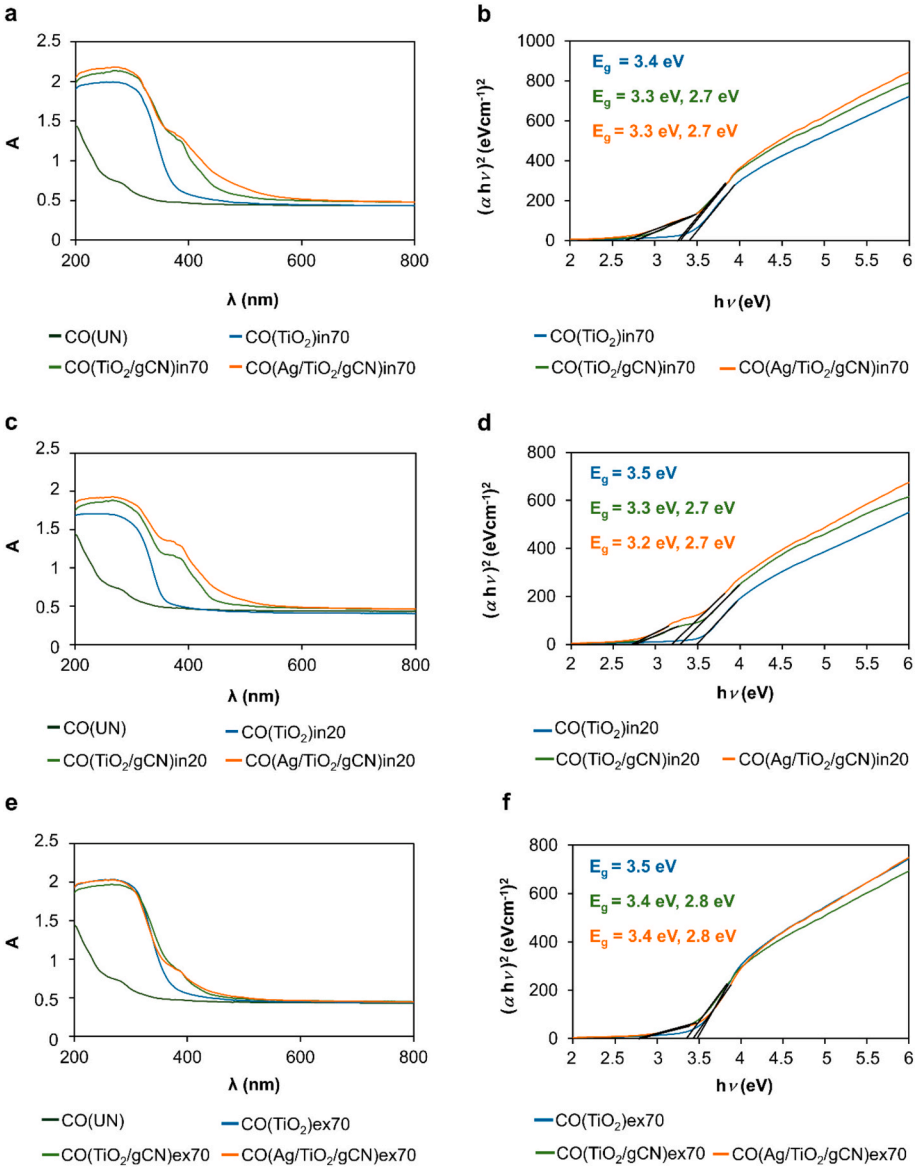

Fig. 9. The absorption spectra (a,c, e) of untreated and chemically modified CO samples synthesised *in situ* at 70 °C (a and b) and 20 °C (c and d) and synthesised *ex situ* at 70 °C (e and f), as well as corresponding Tauc plots (b, d, f).

results are presented in Fig. 9. As the absorption spectra show (Fig. 9(a)), the CO(UN) sample exhibited the lowest absorption intensity over the entire wavelength range measured, indicating its poor light-harvesting capacity. The incorporation of TiO_2 into the CO(TiO_2)in70 sample resulted in increased UV absorption, particularly at wavelengths below 350 nm, which is consistent with the intrinsic band gap absorption of TiO_2.

In contrast, the introduction of gCN and Ag NPs into the nanocomposite structures resulted in a significant increase in visible-light absorption (380–470 nm), as observed for the CO(TiO_2/gCN)in70 and CO(Ag/TiO_2/gCN)in70 samples. These samples also showed increased UV absorption compared to the CO(TiO_2)in70 sample, suggesting synergistic optical effects due to the formation of heterojunctions and the plasmonic properties of the Ag NPs. A similar trend was observed for the samples synthesised *in situ* at 20 °C (Fig. 9(c)), although their overall UV absorbance was notably lower than that of the corresponding samples prepared at 70 °C, probably due to their lower crystallinity. For the samples synthesised *ex situ* at 70 °C (Fig. 9(e)), the main differences in light absorption were observed between 380 and 450 nm. The presence of gCN and Ag NPs in the CO(TiO_2/gCN)ex70 and CO(Ag/TiO_2/gCN)ex70 samples significantly increased the absorbance in this region compared to the CO(TiO_2)ex70 sample, emphasising their role in extending the photoresponse into the visible spectrum.

Tauc plots were derived from the absorption spectra (Equations (2) and (3) and are presented in Fig. 9(b,d,f). The E_g for CO(TiO_2)in70, CO(TiO_2)in20, and CO(TiO_2)ex70 is 3.4 eV, 3.5 eV, and 3.5 eV, respectively, which represents a notably larger band gap than the typical E_g of anatase TiO_2 (~3.2 eV). This widening of the band gap indicates the presence of a significant amount of amorphous TiO_2 in the samples, however, the XRD patterns clearly show characteristic anatase crystal peaks in all powder samples, suggesting the presence of an anatase/amorphous TiO_2 phase mixture. This observation is consistent with the relatively low synthesis temperatures used. The incorporation of gCN and Ag NPs into the nanocomposite structures resulted in a slight red-shift in the band gap, reducing E_g to 3.2–3.4 eV. Consequently, both the two- and three-component nanocomposites exhibited absorption edges at 388–365 nm, independent of the synthesis route and temperature. A closer examination of the Tauc plots revealed an additional inflexion point, which, after extrapolation, corresponds to an E_g in the range of 2.6 ~ 2.8 eV (443–477 nm), which is characteristic of gCN. The latter could be responsible for the increased absorption of visible light in the nanocomposites, which is consistent with the observed absorption spectra.

3.5. Electronic properties and charge carrier dynamics

To determine the influence of gCN and Ag NPs on the charge transfer

Table 3
The average lifetime, $\tau_{average}$, of the entire fluorescence decay process for the signal at the emission wavelength of 446 nm (excitation at 285 nm) and of 360 nm (excitations at 285 nm and 325 nm).

Sample	$\tau_{average,\ int}$ (ns)			$\tau_{average,\ amp}$ (ns)		
	λ_{emi} = 446 nm λ_{exc} = 285 nm	λ_{emi} = 360 nm λ_{exc} = 285 nm	λ_{emi} = 360 nm λ_{exc} = 325 nm	λ_{emi} = 446 nm λ_{exc} = 285 nm	λ_{emi} = 360 nm λ_{exc} = 285 nm	λ_{emi} = 360 nm λ_{exc} = 325 nm
CO(TiO_2) in70	2.5	0.13	0.13	0.5	0.13	0.13
CO(TiO_2/ gCN)in70	6.1	0.16	0.50	1.7	0.16	0.43
CO(Ag/ TiO_2/ gCN)in70	8.0	0.15	0.18	4.1	0.15	0.18

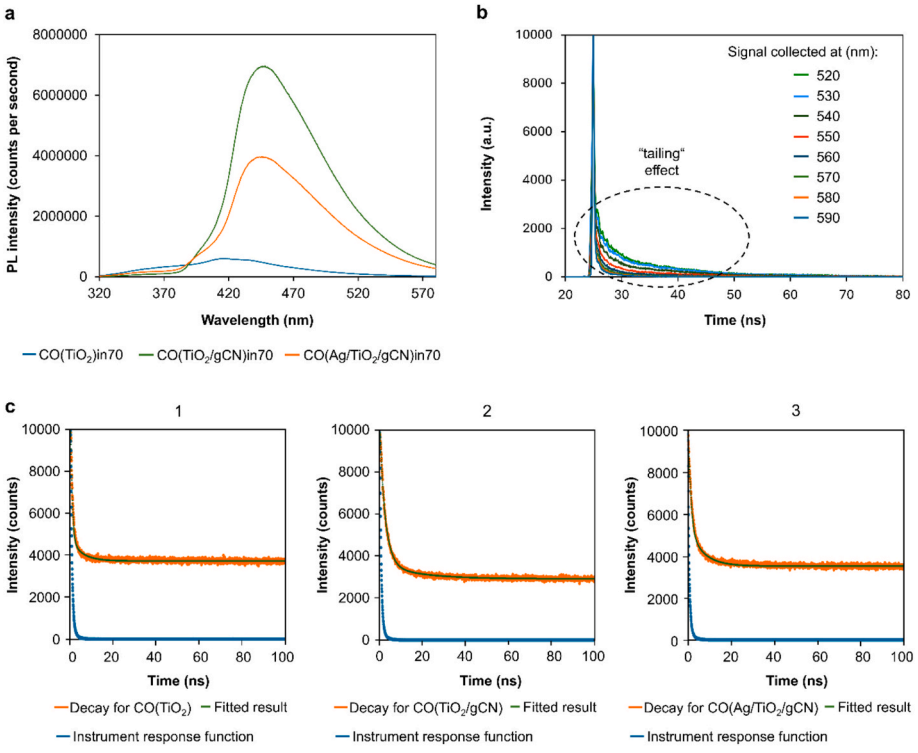

Fig. 10. The steady-state PL spectra of the CO(TiO_2)in70, CO(TiO_2/gCN)in70, and CO(Ag/TiO_2/gCN)in70 samples (excitation at 300 nm) (a). The "tailing" effect observed in the TCSPC measurements, demonstrating the presence of LSPR effects in the CO(Ag/TiO_2/gCN)in70 sample (excitation at 495 nm) (b). TCSPC results of the PL decays of the CO(TiO_2)in70 (c1), CO(TiO_2/gCN)in70 (c2), and CO(Ag/TiO_2/gCN)in70 (c3) samples (excitation at 285 nm, emission at 446 nm; the green lines represent the three-exponential deconvolution fit for the PL decays; the blue dots represent the instrument response function for the pulsed DeltaDiode LED light source at 285 nm).

dynamic in the nanocomposites, the steady-state PL and TCSPC spectra of the CO(TiO_2)in70, CO(TiO_2/gCN)in70, and CO(Ag/TiO_2/gCN)in70 samples were recorded; the results are presented in Fig. 10 and Table 3 [74]. The steady-state PL spectrum of CO(TiO_2)in70 shows characteristic features related to its electronic structure and defects (Fig. 10(a)) [75]. A clear inflexion point appears at 360 nm (3.4 eV), which is due to the end of the band edge emission or shallow defect states near the conduction and valence bands. The main emission peak, centred at about 416 nm (2.98 eV), is generally attributed to the recombination of photogenerated electrons trapped in shallow oxygen vacancy states with holes in the valence band [76]. Alternatively, this emission can also originate from electrons in the conduction band recombining with holes trapped in surface or bulk defects. A weaker and less-well-defined shoulder observed at around 436 nm (2.84 eV) could correspond to deeper trap states or surface-related recombination processes. At longer wavelengths, the PL signal gradually decreases towards zero, which is consistent with the large bandgap of TiO_2.

The PL spectrum of the CO(TiO_2/gCN)in70 sample shows a clear change compared to that of the CO(TiO_2)in70 sample (Fig. 10(a)). The PL intensity of the TiO_2/gCN nanocomposite is initially lower than that of pure TiO_2, indicating a partial suppression of radiative recombination, suggesting an improved separation of photoexcited carriers at the heterojunction surface [77]. The spectrum shows an inflexion point at about 360 nm, which is likely associated with the end of the band edge or flat trap-state emission, in a similar manner as pure TiO_2. A second inflexion point near 395 nm could be related to intermediate defect states at the interface between TiO_2 and gCN or to localised energy levels arising from the formation of the heterojunction. A strong and broad emission peak is observed at about 446 nm (2.78 eV), which is clearly red-shifted compared to the emission of pure TiO_2. This feature is characteristic of gCN and is typically attributed to radiative recombination between photoexcited electrons in the conduction band and holes in the valence band or defect states of gCN [78]. The increased intensity in the composite suggests that gCN plays a dominant role in the emission process and that an efficient energy or charge transfer from TiO_2 to gCN occurs. The monotonic decrease in PL intensity beyond the emission maximum is consistent with typical recombination behaviour and indicates that there is no significant additional emission from the centre of the gap in the visible region.

The PL spectrum of the CO(Ag/TiO_2/gCN)in70 sample exhibits properties that reflect the interplay of radiative recombination and plasmon-induced charge dynamics (Fig. 10(a)). The PL intensity of the Ag/TiO_2/gCN composite is initially intermediate between that of pure TiO_2 and the binary TiO_2/gCN composite, with a turning point at 360 nm, as observed in the previous spectra. This feature is probably related to flat trap-state emission or residual band edge transitions in TiO_2. The prominent emission peak at 446 nm, which is characteristic of gCN-induced radiative recombination, exhibits an intensity about half that of the TiO_2/gCN composite without Ag NPs. This marked attenuation of photoluminescence indicates enhanced charge separation and reduced radiative recombination due to the presence of Ag NPs. The decrease in PL intensity is attributed to the localised surface plasmon resonance (LSPR) effects of the Ag NPs, which facilitates the injection of hot electrons into the conduction bands of TiO_2 and gCN, while acting as an efficient electron sink [79]. This leads to more efficient charge extraction and charge transfer at the Ag/semiconductor interface and suppresses the radiative recombination pathways that generate PL emission.

The PL intensity in the 320–380 nm region is highest for pure TiO_2, lowest for the TiO_2/gCN sample and is in between for the Ag/TiO_2/gCN sample (Fig. 10(a)). This behaviour can be explained by the interplay of charge carrier dynamics and plasmonic effects caused by the Ag NPs. In the case of pure TiO_2, the strong emission in this spectral range is mainly related to band edge transitions and radiative recombination involving flat trap states. The absence of heterojunctions leads to relatively high recombination rates and thus to intense PL emissions. When gCN is combined with TiO_2, the formation of a heterojunction enables more efficient charge separation, which suppresses radiative recombination. This leads to a significant reduction in PL intensity in this region for the TiO_2/gCN composite. After the addition of Ag NPs, the LSPR effects come into play. The enhanced localized electromagnetic field in the vicinity of the Ag particles can increase the excitation probability of charge carriers and thus partially compensate for the reduced radiative recombination caused by the improved charge separation. At the same time, the Ag NPs serve as electron sinks, further promoting charge separation and reducing recombination. As a result, the PL intensity in the 320–380 nm region for the Ag/TiO_2/gCN nanocomposite is at a medium level. It does not decrease as much as for the TiO_2/gCN sample without Ag NPs but remains significantly lower than for pure TiO_2. This balance between plasmonic enhancement and charge separation effects explains the observed trend in PL intensity.

TCSPC was performed on the CO(Ag/TiO_2/gCN)in70 sample to investigate the plasmonic effects associated with LSPR. The TCSPC decay profiles (Fig. 10(b)) showed a pronounced tailing effect in the emission signals recorded at wavelengths below about 580 nm. This tailing is attributed to the LSPR-induced delayed recombination dynamics and the presence of hot electrons generated by plasmonic excitation in the Ag NPs. At wavelengths of 580 nm and above, the tailing effect disappears, suggesting that the plasmonic cloud beyond this range no longer influences hot electron recombination [80]. This wavelength-dependent behaviour confirms the important role of Ag NPs in the modulation of carrier dynamics by plasmonic interactions in the lower wavelength range. Furthermore, the observed clear signal of LSPR strongly suggests that the Ag NPs in the CO(Ag/TiO_2/gCN)in70 sample are most likely present in the metallic (zero-valent) state.

TCSPC measurements were then performed on the CO(TiO_2)in70, CO(TiO_2/gCN)in70, and CO(Ag/TiO_2/gCN)in70 samples; the results are shown in Fig. 10(c) and Table 3. At the emission wavelength of 446 nm, the average amplitude PL lifetimes were determined to be 0.5 ns for TiO_2, 1.7 ns for TiO_2/gCN, and 4.1 ns for Ag/TiO_2/gCN (Table 3). The observed increase in PL lifetime from pure TiO_2 to the TiO_2/gCN nanocomposite indicates a decrease in the recombination rate of photogenerated charge carriers, which is likely due to effective charge separation at the heterojunction interface between TiO_2 and gCN [81,82]. The further extension of the PL lifetime by the incorporation of Ag NPs indicates that the plasmonic effects of metallic Ag NPs not only enhance the charge separation but also stabilize the photogenerated charge carriers by modulating the recombination dynamics. In addition, TCSPC measurements were performed to investigate the charge carrier dynamics at an emission wavelength of 360 nm (Table 3). The measured carrier lifetimes at 360 nm were relatively short for all samples, which, as described above, is consistent with fast recombination processes in shallow defect states or band edge transitions [81,82]. Importantly, the trend observed in TCSPC lifetimes corresponds well with the steady-state PL intensities recorded at this wavelength (Fig. 10(a)). In particular, pure TiO_2 exhibited the shortest lifetimes and the highest PL intensity, indicating higher radiation recombination rates (Table 3) [81]. The TiO_2/gCN nanocomposite showed the longest lifetime and the lowest PL intensity, indicating more efficient charge separation and a suppressed radiative recombination due to heterojunction formation [82]. The Ag/TiO_2/gCN nanocomposite showed intermediate lifetimes and PL intensity, which can be attributed to the competing effects of plasmon-induced carrier dynamics and enhanced charge separation by the Ag NPs. These TCSPC results confirm the steady-state PL results, subsequently confirming that modifications in the material composition directly influence the recombination dynamics of the charge carriers in the emission range of 360 nm.

3.6. Functional properties

3.6.1. Photocatalytic activity and stability

The photocatalytic activity and stability of the chemically modified

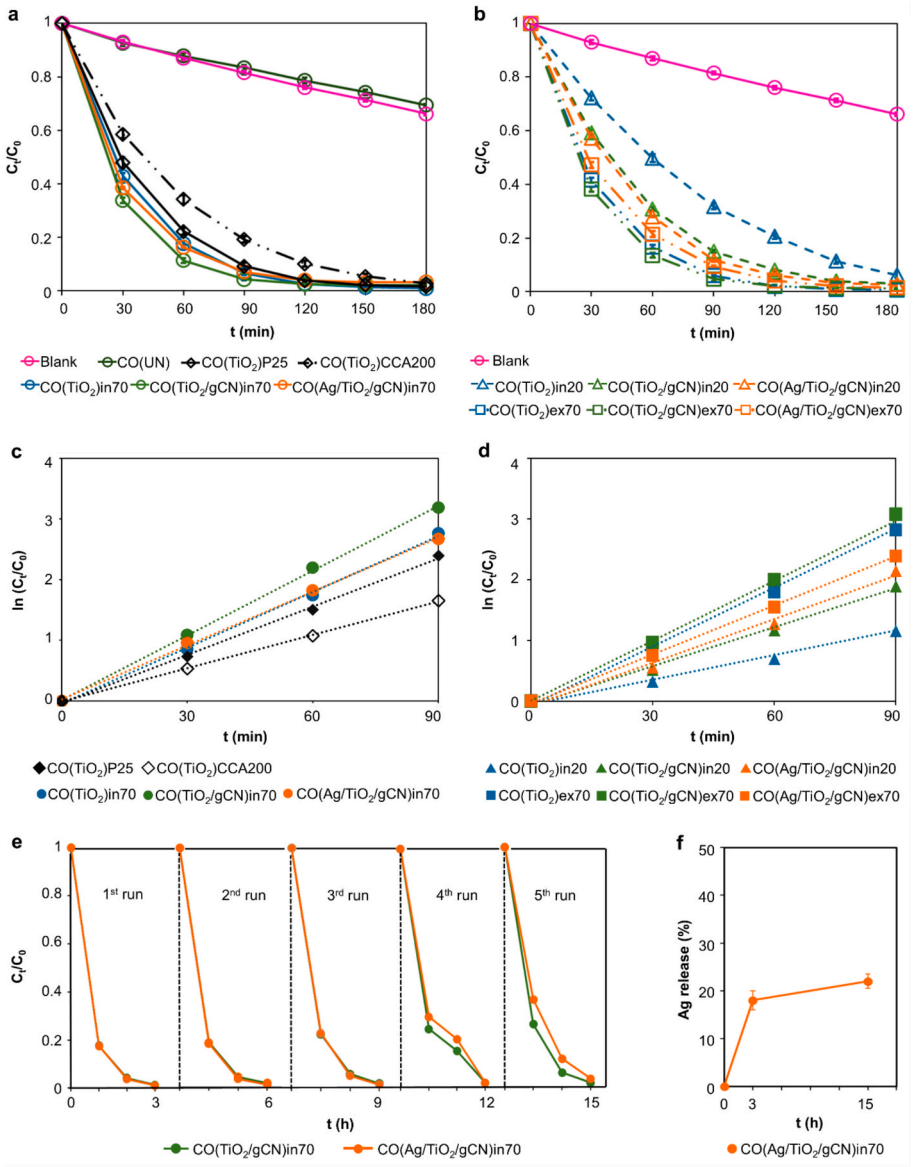

Fig. 11. Decolourisation rate (a and b) and first-order kinetics (c and d) of the RhB dye solution in the presence of untreated and chemically modified CO samples, the reusability experiment (e) of the CO(TiO_2/gCN)in70 and CO(Ag/TiO_2/gCN)in70 samples, as well as the leaching experiment (f) of the CO(Ag/TiO_2/gCN)in70 sample.

Table 4
The decolourisation rate constant, k_{app}, and coefficient of determination, R^2, of the RhB dye solution in the presence of chemically modified CO samples.

Sample	k_{app} (min^{-1})	R^2
CO(TiO_2)in70	3.1×10^{-2}	0.998
CO(TiO_2/gCN)in70	3.6×10^{-2}	0.999
CO(Ag/TiO_2/gCN)in70	3.0×10^{-2}	0.999
CO(TiO_2)in20	1.3×10^{-2}	0.995
CO(TiO_2/gCN)in20	2.1×10^{-2}	0.995
CO(Ag/TiO_2/gCN)in20	2.4×10^{-2}	0.991
CO(TiO_2)ex70	3.1×10^{-2}	0.999
CO(TiO_2/gCN)ex70	3.4×10^{-2}	0.999
CO(Ag/TiO_2/gCN)ex70	2.7×10^{-2}	0.999
CO(TiO_2)P25	2.7×10^{-2}	0.998
CO(TiO_2)CCA200	1.9×10^{-2}	0.999

CO samples were evaluated by monitoring the decolourisation kinetics of the RhB dye solution under solar light irradiation in the presence of the CO samples. The results are presented in Fig. 11 and Table 4. As a reference, control experiments were carried out with the RhB dye solution without CO samples (blank) and in the presence of a CO(UN) sample. The control experiments confirmed the photostability of the RhB dye solution under solar light and achieved an RhB dye degradation of less than 25 % RhB in the presence of the CO(UN) sample after 180 min, indicating that the CO(UN) sample exhibited negligible photocatalytic activity (Fig. 11(a)). In contrast, all chemically modified CO samples achieved the complete (100 %) decolourisation of the RhB dye within the same time period, indicating a significantly increased photocatalytic activity.

A comparative analysis of the photocatalytic efficiency of chemically modified CO samples revealed that the photocatalytic efficiency was primarily influenced by the synthesis temperature and the composition of the CO samples rather than the synthesis route (*in situ* vs. *ex situ*). In particular, the samples synthesised at 20 °C showed a significantly lower photocatalytic activity ($k_{app} = 1.3 \times 10^{-2}$–$2.4 \times 10^{-2}$ min^{-1}) compared to those synthesised at 70 °C, regardless of the synthesis route ($k_{app} = 2.7 \times 10^{-2}$–$3.6 \times 10^{-2}$ min^{-1}) (Fig. 11(b), Table 4). The incorporation of gCN into the TiO_2 matrix significantly increased the photocatalytic

activity of the resulting TiO_2/gCN nanocomposites compared to the pristine TiO_2 at both synthesis temperatures. Of all the samples tested, the CO(TiO_2/gCN)in70 sample showed the highest RhB decolourisation rate, followed by the CO(TiO_2/gCN)ex70 sample.

Furthermore, to validate the photocatalytic efficiency of the TiO_2 synthesised in this work, RhB decolourisation experiments were also performed with CO(TiO_2)P25 and CO(TiO_2)CCA200 reference samples prepared from commercial TiO_2 under identical application conditions as the one-component CO(TiO_2)ex70 sample. As summarised in Table 4, CO(TiO_2)ex70 as well as CO(TiO_2)in70 samples exhibited a superior apparent rate constant ($k_{app} = 3.1 \times 10^{-2}$ min^{-1}) compared to CO(TiO_2)P25 ($k_{app} = 2.7 \times 10^{-2}$ min^{-1}) and CO(TiO_2)CCA200 ($k_{app} = 1.9 \times 10^{-2}$ min^{-1}). The performance was further enhanced by coupling with gCN, emphasising the synergistic contribution of heterojunction formation in the CO(TiO_2/gCN)ex70 and CO(TiO_2/gCN)in70 samples with the k_{app} equals to 3.4×10^{-2} min^{-1} and 3.6×10^{-2} min^{-1}, respectively. Unexpectedly, the incorporation of Ag NPs to form Ag/TiO_2/gCN nanocomposites synthesised at 70 °C resulted in decreased photocatalytic performance in both the CO(Ag/TiO_2/gCN)in70 and CO(Ag/TiO_2/gCN)ex70 samples compared to their Ag-free counterparts.

This finding appears to contradict the results of steady-state and time-resolved PL measurements, which showed that the CO(Ag/TiO_2/gCN)in70 sample exhibits lower PL intensity and a longer carrier lifetime (4.1 ns) than the CO(TiO_2/gCN)in70 sample (1.7 ns), suggesting more efficient charge separation and suppressed electron–hole recombination. This apparent discrepancy emphasises that carrier lifetime alone is not the sole determinant of photocatalytic efficiency; rather, photocatalytic activity arises from a complex interplay between charge-carrier dynamics, surface properties, optical effects, and surface accessibility. It should be noted that a longer carrier lifetime in TRPL does not always imply that carriers are available for surface redox reactions, as non-radiative recombination via trap states can prolong lifetimes without contributing to photocatalysis. Furthermore, the addition of Ag can modify surface chemistry, including surface charge, hydroxyl density, and the adsorption equilibrium of RhB, which can influence the number of reactant molecules available at the active interface. While Ag can in principle enhance photocatalysis through plasmonic hot-electron injection, at higher loadings it may also reduce light penetration due to scattering or parasitic absorption by metallic domains, depending on particle size, shape, and overlap with the irradiation spectrum [83]. The quantitative connection between PL lifetime and photocatalytic turnover is not direct, as PL primarily probes radiative recombination in bulk or near-surface regions, whereas photocatalysis occurs at the solid–liquid interface. Although the presence of Ag facilitates charge separation in the CO(Ag/TiO_2/gCN)in70 composite, extensive Ag loading can partially block active semiconductor surface sites, thereby decreasing the number of accessible surface oxidation sites and offsetting the advantages associated with extended carrier lifetimes. Similar trends have been reported previously for TiO_2 systems with higher concentrations of noble metals [84,85]. It should also be noted that in the present work, the Ag content in the Ag/TiO_2/gCN composites was not optimised solely for photocatalytic activity but was deliberately chosen to balance photocatalytic and antibacterial functionalities, ensuring the multifunctional performance of the CO samples. In contrast, incorporating Ag NPs into the CO(Ag/TiO_2/gCN)in20 sample, synthesised at 20 °C, enhanced photocatalytic activity compared to the CO(TiO_2/gCN)in70 sample. A similar trend was observed for the *ex situ* synthesised composites at 20 °C [86]. These findings suggest that, in addition to Ag concentration, the synthesis temperature is crucial in determining the structural and interfacial characteristics of the nanocomposites, significantly influencing their photocatalytic efficiency.

To ensure the reliability of the photocatalytic data and quantitatively assess the efficiency of incident photons in driving the photocatalytic reaction, the rate constants (k_{app}) for RhB dye decolourisation obtained from the most efficient samples–CO(TiO_2/gCN)in70 and its Ag containing counterpart CO(Ag/TiO_2/gCN)in70–were normalised to photon flux, allowing calculation of the apparent quantum efficiency (*AQE*). These values were compared with that of the CO(TiO_2)P25 sample, in which commercially available Degussa TiO_2 P25, as a commercially available mixed anatase/rutile phase composite, was used as a reference benchmark due to its well-established high photocatalytic activity and extensive characterisation in the literature. The *AQE* was determined according to the following equation [87,88]:

$$AQE(\%) = \left(\frac{r_0}{n_{ph}}\right) \times 100 = \left(\frac{k_{app} C_o V}{n_{ph}}\right) \times 100 \quad (9)$$

where r_0 represents the initial rate of RhB dye degradation (expressed as the number of molecules or moles converted per second), corresponding to the number of electrons required by the reaction product, and n_{ph} denotes the number of incident photons absorbed by the reacting system per second. The calculated *AQE* values were 54.3 % for CO(TiO_2/gCN)in70 and 35.5 % for CO(Ag/TiO_2/gCN)in70, both significantly higher than the 10.7 % obtained for the CO(TiO_2)P25 reference sample (Section S5, Eqs. (S9) and (S10), and Table S5, Supplementary material). These results demonstrate the superior photocatalytic efficiency of the TiO_2/gCN-based nanocomposites compared with the benchmark TiO_2 P25 material.

To evaluate the stability and reusability of the nanocomposites, the CO(TiO_2/gCN)in70 sample, which was identified as the most photocatalytic-efficient sample, and the Ag-containing CO(Ag/TiO_2/gCN)in70 sample were used in five replicate experiments for the decolourisation of RhB (Fig. 11(e)). Both samples exhibited a high stability and reusability, resulting in a 100 % degradation of the RhB dye after 180 min of irradiation in each run. In the first three runs, there was no difference in the decolourisation rate between the samples. After the fourth run, a slight difference in decolourisation efficiency was obtained, with the CO(TiO_2/gCN)in70 sample showing a faster decolourisation rate than the CO(Ag/TiO_2/gCN)in70 sample after 60 and 120 min. However, RhB decolourisation was completed after 180 min for both samples. To confirm the Ag/TiO_2/gCN coating stability, Ag leaching from the CO(Ag/TiO_2/gCN)in70 sample was quantified by ICP–OES under the same conditions used during the reusability test. The results show that 18 % of the deposited Ag was released within 3 h (1st run), while extending the immersion time to 15 h (5th run) led to only a minor additional release reaching 22 % (Fig. 11(f)). This minimal change (4 % in 12 h) indicates that Ag release rapidly reaches a plateau and establishes the control-release mechanism. The long-term stability and durability of both the CO(TiO_2/gCN)in70 and CO(Ag/TiO_2/gCN)in70 the CO samples were also confirmed by EDS analysis and elemental mapping after the third and fifth runs (Section S4, Figs. S11 and S12, Supplementary Material). The EDS spectra and corresponding elemental mapping showed the consistent presence of C, O, Ti, and N in both samples, while Ag was retained in the CO(Ag/TiO_2/gCN)in70 sample even after the fifth run. These results demonstrate strong interfacial coupling of the nanocomposites to the cellulose backbone, yielding a robust and durable photocatalytic platform. This is further supported by the XPS results, which corroborate the interfacial stability of the composites.

To elucidate the mechanism of RhB dye decolourisation and to verify the generation of reactive oxygen species (ROS) and photogenerated holes (h^+) in the CO(TiO_2/gCN)in70 and CO(Ag/TiO_2/gCN)in70

Table 5
The decolourisation rate constant, k'_{app}, of the RhB dye solution containing BQ, EDTA-2Na, and IPA as scavengers in the presence of the CO(TiO_2/gCN)in70 and CO(Ag/TiO_2/gCN)in70 samples.

Sample	k'_{app}(min^{-1})		
	BQ	EDTA-2Na	IPA
CO(TiO_2/gCN)in70	1.3×10^{-2}	1.0×10^{-2}	3.1×10^{-2}
CO(Ag/TiO_2/gCN)in70	6.8×10^{-3}	1.9×10^{-2}	2.8×10^{-2}

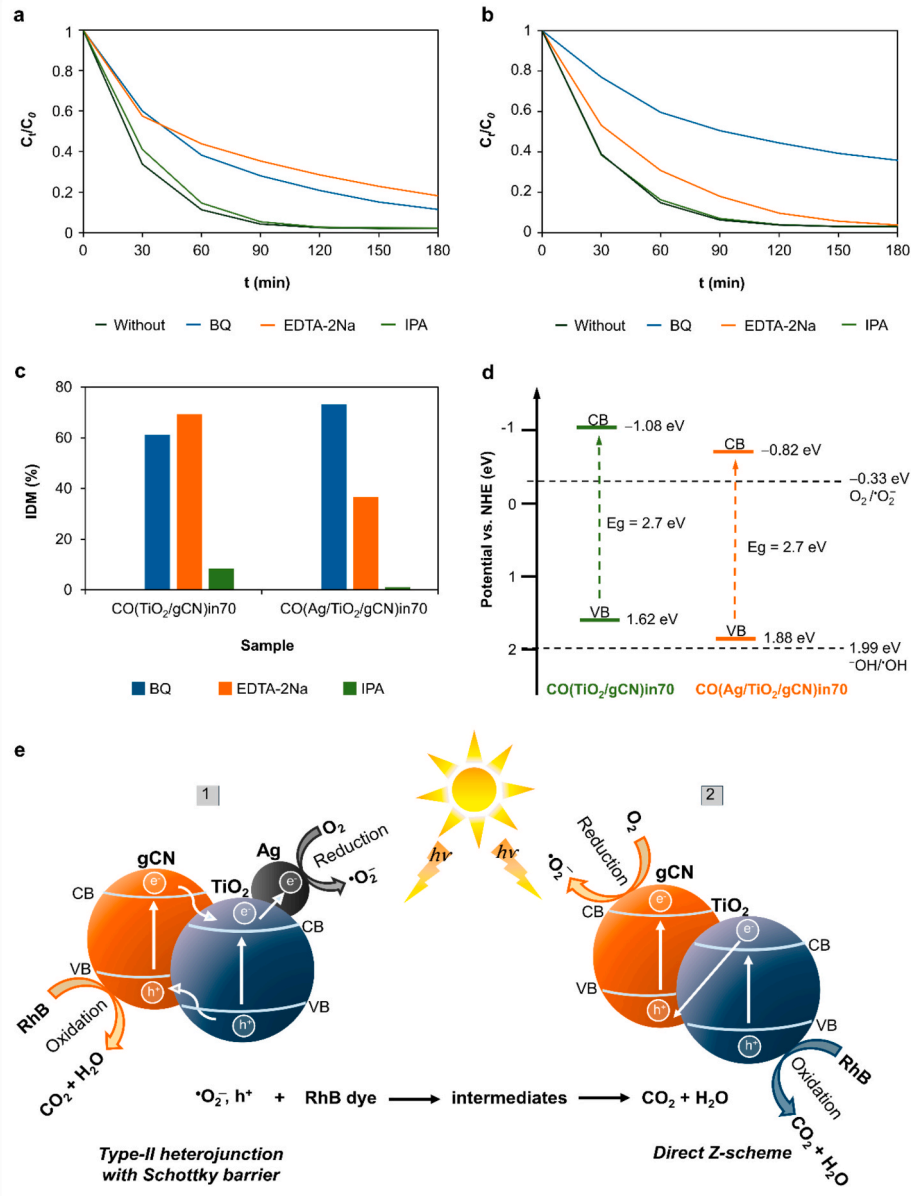

Fig. 12. The scavenging experiment of photogenerated ROS and h^+ formed on CO(TiO_2/gCN)in70 (a) and CO(Ag/TiO_2/gCN)in70 (b), the importance of the decolourisation mechanism (IDM) (c), schematic diagrams of the energy band structure for CO(TiO_2/gCN)in70 and CO(Ag/TiO_2/gCN)in70 (d), and the anticipated photocatalytic mechanisms of CO(Ag/TiO_2/gCN)in70 (e1) and CO(TiO_2/gCN)in70 (e2).

samples, a series of ROS scavenging experiments were performed (Table 5, Fig. 12). The addition of IPA had no significant influence on the decolourisation rate of the RhB dye, indicating that $^{\bullet}OH$ radicals play a negligible role in the photocatalytic mechanism of both the CO(TiO_2/gCN)in70 and CO(Ag/TiO_2/gCN)in70 samples (Fig. 12(a,b)). This observation is somewhat unexpected, since the VB edge potential of TiO_2 anatase (+2.91 eV vs. NHE) is sufficiently positive relative to the $^{-}OH/^{\bullet}OH$ redox potential (+1.99 eV), which thermodynamically permits the generation of $^{\bullet}OH$ radicals via the oxidation of surface-adsorbed water by photogenerated h^+ [89]. Nonetheless, similar results were obtained when other $^{\bullet}OH$ radical scavengers, such as *tert*-butyl alcohol and ethanol, were employed, further supporting the limited involvement of $^{\bullet}OH$ radicals in the RhB degradation pathway. In contrast, the presence of BQ and EDTA-2Na markedly hindered the decolourisation efficiency, implying that $^{\bullet}O_2^-$ and h^+ are the primary reactive species involved in the photocatalytic decolourisation of RhB in both photocatalysts. However, the underlying photocatalytic mechanisms differ between the two samples (Fig. 12(c)). Specifically, in the case of the CO(TiO_2/gCN)in70 sample, the IDM values observed in the presence of the BQ and EDTA-2Na scavengers are similar, suggesting that $^{\bullet}O_2^-$ and h^+ contributed equally to the photocatalytic process. In contrast, for the CO(Ag/TiO_2/gCN)in70 sample, the IDM value in the presence of BQ was more than twice that observed with EDTA-2Na, indicating that the decolourisation of RhB is predominately mediated by $^{\bullet}O_2^-$. The ROS scavenging assays, in combination with UV–Vis spectroscopy and fluorescence and TCSPC measurements, demonstrate that band gap–driven electron–hole excitation under irradiation directly governs charge carrier generation, lifetime and recombination dynamics, providing definitive evidence for ROS production and the associated photophysical processes.

To further clarify the electronic structure of the CO(TiO_2/gCN)in70 and CO(Ag/TiO_2/gCN)in70 samples and to identify which surface redox processes are energetically accessible, the ionisation potential (*IP*) was determined from the UPS analysis. The *IP* represents the minimum energy required to remove an electron from the valence band maximum (VBM) to the vacuum level and was calculated using Eq. (10):

$$IP = h\nu - \left(E_{\text{cutoff}} - E_{\text{VBM}}\right) \quad (10)$$

where E_{cutoff} corresponds to the secondary electron cutoff, and E_{VBM} denotes the valence-band onset extracted from the UPS spectra (Figs. S13 and S14, Section S6, Supplementary Material). From the IP values, the absolute VBM positions were referenced to the vacuum level, and the corresponding conduction band minima (CBM) were estimated using the optical bandgaps (E_g) obtained from the Tauc plots (Fig. 9(b)). After converting the vacuum-referenced energies to the normal hydrogen electrode (NHE) scale (Section S6, Eqs. (S11)–(S14), Supplementary Materials), the valence and conduction band positions of both nanocomposites are shown in Fig. 12(d).

These band-edge potentials define the redox reactions that are thermodynamically assesible at the nanocomposite surface. Since the CBM of both CO(TiO_2/gCN)in70 and CO(Ag/TiO_2/gCN)in70 is more negative than the $O_2/^{\bullet}O_2^-$ potential (−0.33 eV), the photogenerated electrons are capable of reducing O_2 to $^{\bullet}O_2^-$. The more negative CBM of CO(TiO_2/gCN)in70 relative to CO(Ag/TiO_2/gCN)in70 indicates a higher electron-reducing capacity, which can facilitate electron-driven reduction pathways and consequently contribute to enhanced photocatalytic performance of the nanocomposite. Conversely, the VBM positions of both nanocomposites is less positive than the $^{\bullet}OH/^{-}OH$ redox potential (+1.99 eV), implying that direct generation of $^{\bullet}OH$ radicals via oxidation of $^{-}OH/H_2O$ is not thermodynamically favourable. This interpretation aligns with the observations from the radical scavenging experiments, which confirmed the limited involvement of $^{\bullet}OH$ in the photocatalytic mechanism.

Based on the decolourisation results, the results of the PL measurements and the UPS analysis, two distinct photocatalytic mechanisms are proposed for the CO(TiO_2/gCN)in70 and CO(Ag/TiO_2/gCN)in70 samples (Fig. 12(e)) [90,91]. For the CO(Ag/TiO_2/gCN)in70 sample, the photocatalytic process is believed to follow the Type-II heterojunction between TiO_2 and gCN, coupled with the formation of a Schottky barrier at the Ag/TiO_2 interface (Fig. 12(e1)). Under simulated solar irradiation, both TiO_2 and gCN are photoexcited, promoting electrons (e^-) from the valence band (VB) to the conduction band (CB), leaving holes (h^+) in the VB. While gCN predominantly absorbs visible light, TiO_2 is activated under UV illumination. Due to the more-negative CB edge potential of gCN than that of TiO_2, the photogenerated e^- can be easily transferred from the CB of gCN to the CB of TiO_2. Simultaneously, photogenerated h^+ are transferred from the VB of TiO_2 to the VB of gCN, as the VB edge potential of TiO_2 is more positive than that of gCN. The accumulated e^- in the CB of TiO_2 are further transferred to Ag NPs, facilitated by the lower Fermi level of Ag relative to TiO_2. This results in the formation of a Schottky barrier, which enhances the charge carrier separation and suppresses recombination. The trapped e^- in Ag NPs readily participate in surface reduction reactions, leading to the formation of $^{\bullet}O_2^-$, which has been identified as the dominant ROS responsible for the RhB dye decolourisation, as confirmed by scavenging experiments. Additionally, visible-light irradiation induces LSPR excitation in Ag NPs, further enhancing photocatalytic activity via plasmon resonance energy transfer. Despite the improved photocatalytic performance of the CO(Ag/TiO_2/gCN)in70 nanocomposite compared to cotton modified solely with TiO_2, its primary limitation lies in the oxidative pathway. Hole-driven oxidation reactions predominantly occur on gCN, which possesses a lower oxidation potential compared to TiO_2 [34,90,91]. Consequently, the contribution of photogenerated h^+ to the overall RhB degradation is limited, in agreement with the results of the scavenging experiment.

For the CO(TiO_2/gCN)in70 sample, a distinctly different charge carrier transfer pathway is proposed, as illustrated in Fig. 12(e2). Since both $^{\bullet}O_2^-$ and photogenerated h^+ contribute significantly to the photocatalytic activity, it is postulated that photogenerated e^- excited into the CB of TiO_2 undergo recombination with photogenerated h^+ in the VB of gCN, which exhibit a lower redox ability [90,92]. This charge recombination facilitates the spatial separation of the remaining charge carriers while e^- remains in the CB of gCN, which has a higher reduction potential, and h^+ remains in the VB of TiO_2, which has a higher oxidation potential. In this configuration, the photogenerated e^- in the CB of gCN efficiently reduce molecular oxygen adsorbed on the nanocomposite, generating reactive $^{\bullet}O_2^-$ species that participate in secondary oxidation steps leading to the RhB dye degradation. Simultaneously, the photogenerated h^+ in the VB of TiO_2 directly oxidise RhB molecules. This charge separation pathway ensures strong redox capability, which is consistent with the observed high photocatalytic efficiency in RhB dye decolourisation. The proposed mechanism closely resembles a direct Z-scheme heterojunction, as reported in the literature [13,89,90,92–94]. However, the key distinction in this system lies in the oxidation mechanism, whereby the photogenerated h^+ in the VB of TiO_2 predominantly facilitate the direct oxidation of the RhB dye rather than initiating the formation of $^{\bullet}OH$ radicals, as supported by the results of the $^{\bullet}OH$ radical scavenging experiments.

3.6.2. *UV protection properties*

The UV protection performance of the CO samples was evaluated based on their transmission spectra in the wavelength range of 280–400 nm; the results are presented in Fig. 13. It is evident that the transmission spectra are directly related to the absorption spectra (Fig. 9(a,c,e)), as the absorbance at specific UV wavelengths indicates how much UV light is attenuated by the material. Higher absorbance in the UV region corresponds to a greater ability to block or absorb UV rays, resulting in improved UV-shielding performance. The optical bandgaps of the chemically modified CO samples, which are 3.5–3.2 eV (Fig. 9(b,d,f)), correspond to the UVA range and indicate that all samples can efficiently absorb UV photons.

The results show that the unmodified CO(UN) sample exhibited the highest optical transmittance over the entire spectral range (Fig. 13(a)), resulting in the lowest UV-A (Fig. 13(b)) and UV-B (Fig. 13(c)) blocking effect. Consequently, the UPF value (Fig. 13(d)) did not meet the minimum protection defined by the Australian/New Zealand Standard. As expected, the chemical modification of the CO samples led to a notable reduction in UV transmittance, primarily due to the incorporation of TiO_2, which is a well-known UV absorber with a greater attenuation effect in the UV-B region than in the UV-A region (Fig. 13(a)). All chemically modified CO samples showed an excellent UV-B blocking effect of over 97 % (Fig. 13(c)). The incorporation of gCN and Ag NPs into the nanocomposite matrix led to a significant reduction in UV-A transmittance (Fig. 13(a,b)), consistent with the redshifts in the absorption edge (Fig. 9(b,d,f)). This enhanced UV absorbance in the UVA region, thereby increasing shielding performance. This clearly confirms the synergistic contribution of gCN and Ag NPs to UV-A absorption, which improves the overall UV shielding performance of the nanocomposites.

The UPF values of the chemically modified CO samples indicate that the UV protection performance is not only influenced by the chemical composition of the samples, but also by the synthesis temperature and the synthesis route used (Fig. 13(d)). For example, the CO(TiO_2)in20 sample synthesised at 20 °C had a UPF of 21, which corresponds to minimal UV protection. In contrast, increasing the synthesis temperature to 70 °C significantly increased the effectiveness of UV protection and resulted in UPF values of 44 and 40 for the CO(TiO_2)in70 and CO(TiO_2)ex70 samples, respectively, both of which are categorised as good UV protection. In particular, *in situ* synthesis at 70 °C resulted in superior UV protection, with the CO(TiO_2/gCN)in70 and CO(Ag/TiO_2/gCN)in70 samples achieving UPF values of 85 and 90, respectively. These values are almost twice as high as those of the corresponding samples synthesised either *in situ* at 20 °C or *ex situ* at 70 °C. Of all the samples, CO(Ag/TiO_2/gCN)in70 exhibits the highest UV shielding efficiency, with UV-A and UV-B blocking efficiencies of 96.5 and 99.2 %, respectively. These results highlight the crucial role of the synthesis parameters, particularly in relation to the *in situ* route at elevated temperature (70 °C), in optimising the performance of Ag/TiO_2/gCN

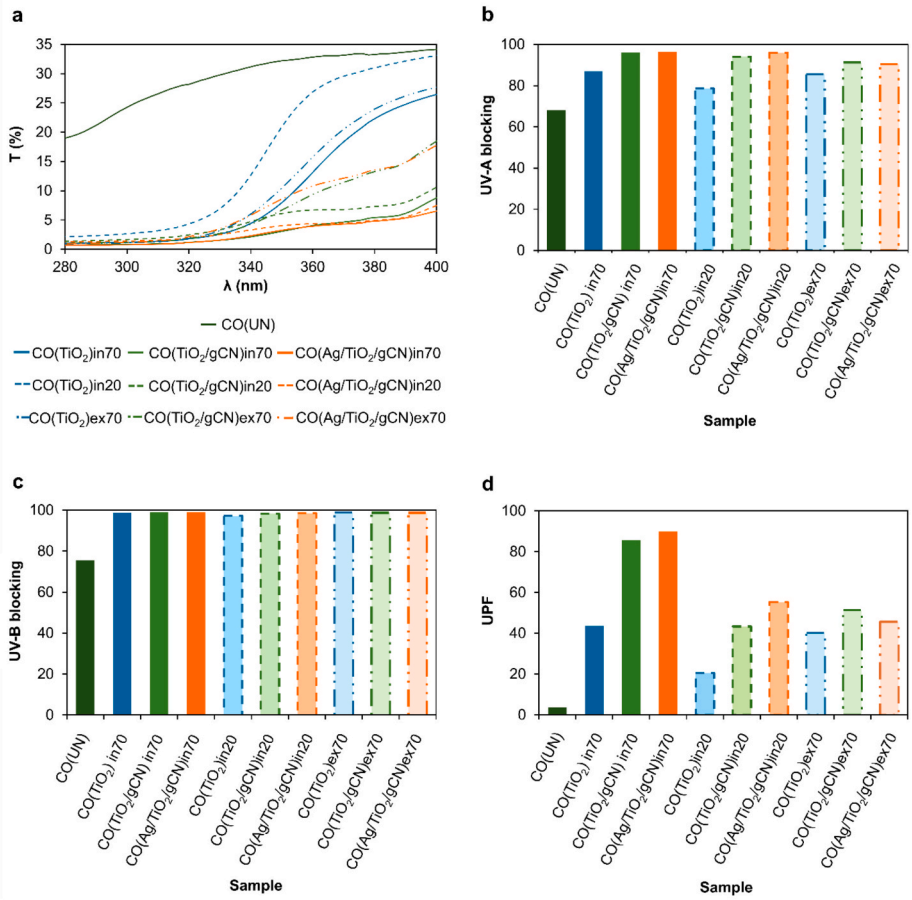

Fig. 13. Transmission spectra (a). UV-A (b) and UV-B (c) blocking and UPF (d) capabilities for the untreated and chemically modified CO samples.

nanocomposites. The resulting textile materials show great potential for application in UV protection textiles with excellent blocking capacity in both the UV-A and UV-B range.

3.6.3. *Antibacterial activity and cytotoxicity*

The antibacterial activity of both the untreated and the chemically modified CO samples was analysed against Gram-positive bacteria *S. aureus* and Gram-negative bacteria *E. coli*. The results are presented in Fig. 14 together with the corresponding cytotoxicity data. The antibacterial efficiency of the studied nanocomposites is attributed to the combined effects of the intrinsic antimicrobial mechanisms of noble metals and photocatalytic materials, as well as their synergistic interactions within the composite structure. Specifically, the antimicrobial activity of Ag is associated with the controlled release of Ag^{+} ions and the action of Ag NPs, which bind to bacterial cell membranes and induce structural alterations, penetrate the cytoplasm, and interact with thiol-containing proteins, leading to enzyme inhibition and disruption of DNA replication [95]. In contrast, TiO_2 functions primarily as a photocatalyst, exerting its antibacterial effects through the generation of ROS. Upon light activation, these ROS can permeate bacterial cell walls and

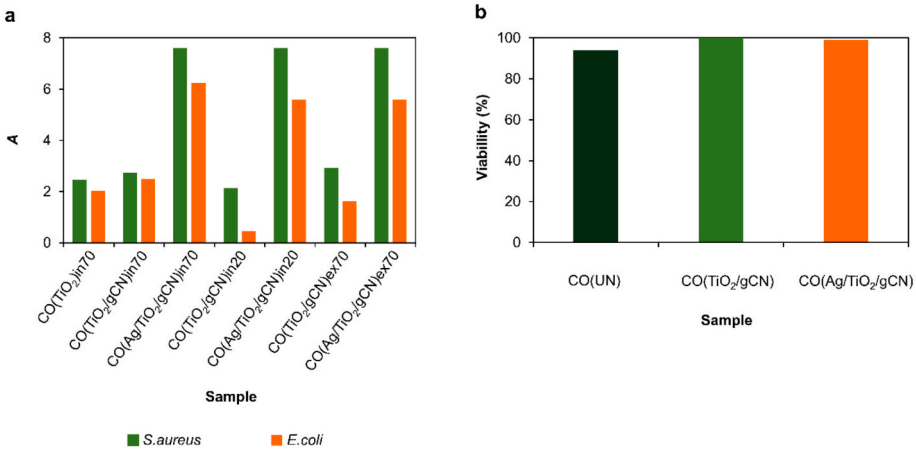

Fig. 14. The antibacterial activity value, *A*, of chemically modified CO samples (a); the viability of cells in contact with the CO(UN), CO/(TiO_2/gCN)in70, and CO/(Ag/TiO_2/gCN)in70 samples (b).

induce oxidative damage to essential biomolecules, including lipids, proteins, and nucleic acids, thereby compromising cellular integrity and viability [5,96,97].

As shown in Fig. 14(a), all samples exhibited a higher antimicrobial activity against *S. aureus* than against *E. coli*, which illustrates the different resistance mechanisms in combination with the structural differences in the bacterial cell envelopes. Specifically, Gram-negative bacteria have a thin peptidoglycan layer surrounded by an outer membrane that is rich in lipopolysaccharides. This outer layer acts as an effective permeability barrier that reduces the diffusion of antimicrobial agents and contributes to the higher intrinsic resistance of *E. coli*. In contrast, Gram-positive bacteria lack an outer membrane and instead possess a thick peptidoglycan layer, which in some cases can be more accessible to certain antimicrobial agents. This structural feature facilitates the adsorption and interaction of nanoparticles and active species, making *S. aureus* more susceptible to antibacterial treatments [96].

As shown in Fig. 14(a), the photogenerated ROS in TiO_2 and TiO_2/gCN significantly contributed to the antibacterial performance of the CO(TiO_2)in70, CO(TiO_2/gCN)in70, CO(TiO_2/gCN)in20, and CO(TiO_2/gCN)ex70 samples. The enhanced antibacterial activity of CO(TiO_2/gCN)in70 compared to CO(TiO_2)in70 is attributed to the synergistic action of TiO_2 and gCN in the nanocomposite, which exhibited increased ROS formation and extended light absorption, as confirmed by the photocatalytic experiment. The incorporation of Ag NPs into the Ag/TiO_2/gCN nanocomposites led to a significant increase in the antibacterial activity of the samples, regardless of the synthesis temperature or the synthesis route. Remarkably, even the CO(Ag/TiO_2/gCN)ex70 sample, which contained only traces of Ag NPs, exhibited more than twice the *A* value against both *S. aureus* and *E. coli* than the silver-free counterpart CO(TiO_2/gCN)ex70. This clearly indicates the synergistic antibacterial effect of Ag NPs, TiO_2, and gCN within the nanocomposite structure through a dual-action mechanism, including Ag^+ release and ROS formation, which provides broad-spectrum, long-lasting antibacterial performance. Furthermore, increasing the Ag NPs content from 50 mg/kg to 200 mg/kg in the CO(Ag/TiO_2/gCN)in70 sample resulted in the maximum biocidal activity, with *A* values of $\log_{10}$ CFU of 7.6 and 6.3 for *S. aureus* and *E. coli*, respectively, which corresponds to complete bacterial inhibition, with no detectable CFUs. This strong antibacterial effect is attributed to the combined action of Ag^+ and Ag nanoparticles, both of which exert multiple targeting mechanisms, ultimately leading to complete bacterial cell death.

To assess the biocompatibility of the chemically modified CO samples and their suitability for applications involving contact with human tissue, *in vitro* cytotoxicity assays were conducted using the CO(TiO_2/gCN)in70 and CO(Ag/TiO_2/gCN)in70 samples, which contained the highest concentrations of TiO_2 (12,000 mg/kg) and Ag (200 mg/kg), respectively. The CO(UN) sample served as a reference control. As shown in Fig. 14(b), none of the tested samples exhibited cytotoxic effects. The CO(UN) sample demonstrated a cell viability of 94 %, whereas the CO(TiO_2/gCN)in70 and CO(Ag/TiO_2/gCN)in70 samples showed enhanced viability of 100 % and 99 %, respectively. This suggests that the incorporation of the amorphous TiO_2 fraction may contribute to improved cytocompatibility, probably due to the lower crystalline surface reactivity. Moreover, the Ag content in the CO(Ag/TiO_2/gCN)in70 sample remains below the cytotoxicity threshold, thereby preserving cellular viability.

Ag leaching experiments (Fig. 11(f)) further corroborate the stability and safety of the CO(Ag/TiO_2/gCN) sample. After 3 h of immersion in water, only 18 % of the initially deposited Ag was released (4.14 mg/L), with a minimal increase to 22 % (an additional 0.92 mg/L) after 15 h, indicating that most Ag is strongly immobilised on the fibre surface and that leaching rapidly reaches a plateau. This controlled release behaviour, combined with cytotoxicity results demonstrating 100 % cell viability and antimicrobial assays showing total bacterial inhibition with no detectable CFUs, confirms that this sample is both non-cytotoxic and highly effective against microbial contamination. The observed safety is attributed to chemical bonding of the nanocomposite to the CO substrate, which limits Ag^+ ion release and mitigates potential toxicity. The combined effect of controlled Ag release, stable nanocomposite bonding, and ROS-mediated photocatalysis ensures both high cytocompatibility and robust antimicrobial performance, consistent with previous reports even at higher Ag concentrations [98,99], thereby confirming the long-term safety and functional efficacy of these materials for biomedical and protective textile applications.

4. Conclusions

In this study, Ag/TiO_2/gCN nanocomposites with multifunctional properties—photocatalytic performance, UV shielding, and antibacterial activity—were developed for the first time on CO fabric using a facile ultrasound-assisted sol–gel synthesis method. The influence of the chemical composition, synthesis temperature, and the synthesis route on the physicochemical and functional properties of the resulting nanocomposites was systematically investigated.

The Ag/TiO_2/gCN nanocomposites exhibited a mesoporous architecture consisting of gCN nanosheets, a mixed phase of anatase and amorphous TiO_2, and face-centred cubic Ag NPs. Synthesis at 70 °C resulted in nanocomposites with a slightly reduced pore size and volume compared to those synthesised at 20 °C. This indicates faster sol–gel network condensation and cross-linking at higher temperatures, which favoured the formation of denser structures with fewer and smaller pores. Furthermore, *in situ* synthesis at 70 °C in the presence of the CO substrate significantly improved the loading of both TiO_2 and Ag components compared to *in situ* synthesis at 20 °C or *ex situ* synthesis at 70 °C.

The nanocomposites synthesised at 20 °C exhibited a significantly lower photocatalytic activity than those synthesised at 70 °C, regardless of the synthesis route. The incorporation of gCN into the TiO_2 matrix significantly enhanced the photocatalytic activity of the resulting nanocomposites compared to pristine TiO_2 at both synthesis temperatures. At 20 °C, the addition of Ag NPs further improved the photocatalytic performance compared to the binary TiO_2/gCN nanocomposite; however, this improvement was not observed for the nanocomposite synthesised at 70 °C. These results indicate that the synthesis temperature plays a crucial role in determining the construction, and consequently, the photocatalytic efficiency of the nanocomposites. The photocatalytic mechanism of the Ag/TiO_2/gCN nanocomposite synthesised at 70 °C presumably follows a Type-II heterojunction between TiO_2 and gCN, coupled with the formation of a Schottky barrier at the Ag/TiO_2 interface, which is enhanced by the LSPR effect of Ag NPs. However, this mechanism appeared to be slightly less effective than the Z-scheme mechanism proposed for the TiO_2/gCN nanocomposite synthesised under the same conditions.

The incorporation of gCN and Ag NPs, together with an increase in the synthesis temperature and the transition from an *ex situ* to an *in situ* synthesis route, significantly increased the UV shielding performance of the nanocomposites. In particular, the nanocomposite synthesised *in situ* at 70 °C exhibited a UPF of 90, almost twice as high as those of the nanocomposites synthesised either *in situ* at 20 °C or *ex situ* at 70 °C.

The presence of Ag NPs in the Ag/TiO_2/gCN nanocomposites markedly improved the antibacterial activity, regardless of the synthesis temperature or route. Increasing the Ag NPs content led to a maximum biocidal performance in the nanocomposite synthesised *in situ* at 70 °C, resulting in complete bacterial inactivation of *S. aureus* and *E. coli*, with no detectable viable colonies, corresponding to $\log_{10}$ CFU reductions (*A* values) of 7.6 and 6.3, respectively. These findings clearly demonstrate a synergistic antibacterial effect that results from the combined action of Ag NPs, TiO_2, and gCN within the nanocomposite matrix.

The Ag/TiO_2/gCN nanocomposites demonstrated excellent cytocompatibility. In particular, the nanocomposite synthesised *in situ* at 70 °C, which contained the highest concentrations of TiO_2 (12,000 mg/kg) and Ag NPs (200 mg/kg), showed a cell viability of 99 %. These

results indicate that the Ag NPs content remained below the cytotoxicity threshold and that the incorporation of the amorphous TiO_2 fraction may contribute to improved cytocompatibility. This indicates the potential for the safe application of the chemically modified CO samples in various textile-related areas.

In summary, all components comprising the ternary Ag/TiO_2/gCN nanocomposite are essential for achieving multifunctionality, including photocatalytic activity, UV protection, and antibacterial performance. The synergistic interactions between Ag NPs, TiO_2, and gCN play a key role in enhancing these functional properties. Furthermore, the synthesis strategy has a strong influence on the performance of the nanocomposite, where *in situ* synthesis route at elevated temperatures is preferable to ensure the effective loading of the nanocomposites.

CRediT authorship contribution statement

Dominika Glažar: Writing – original draft, Visualization, Validation, Investigation, Formal analysis, Data curation. **Brigita Tomšič:** Writing – review & editing, Formal analysis, Investigation. **Ivan Jerman:** Writing – review & editing, Formal analysis, Investigation, Resources. **Raghuraj S. Chouhan:** Writing – review & editing, Resources. **Andraž Šuligoj:** Writing – review & editing, Investigation, Formal analysis. **Matija Zorc:** Writing – review & editing, Investigation, Formal analysis. **Albin Pintar:** Writing – review & editing, Resources, Investigation, Funding acquisition, Formal analysis. **Janez Kovač:** Writing – review & editing, Investigation, Formal analysis. **Andraž Krajnc:** Writing – review & editing, Resources, Investigation. **Francisco Ruiz-Zepeda:** Writing – review & editing, Investigation, Formal analysis. **Barbara Simončič:** Writing – review & editing, Supervision, Resources, Methodology, Funding acquisition, Conceptualization.

Declaration of competing interest

The authors declare that they have no known competing financial interests or personal relationships that could have appeared to influence the work reported in this paper.

Acknowledgements

This work was supported by the Slovenian Research and Innovation Agency (Programmes P2-0213, P1-0021, P1-0134, P1-0195, P1-0418, P2-0082, P2-0150, P2-0393, BI-US/22-24-162, Infrastructural Centre RIC UL-NTF and a Grant for the doctoral student D.G.). The authors would like to thank Prof. Dr. Matej Dolenec for XRD measurements, Dr. Matic Šobak for the SEM measurements, Janez Volavšek for NMR measurements, Dr. Tecush Mohammadi for the constructive discussion and the assessment of the apparent quantum efficiency, and Assist. Dr. Barbara Golja for her support in operating the Xenotest Alpha instrument.

Appendix A. Supplementary data

Supplementary data to this article can be found online at https://doi.org/10.1016/j.apsusc.2025.165446.

Data availability

Data will be made available on request.

References

[1] M. Akbar Shah, B.M. Pirzada, G. Price, A.L. Shibiru, A. Qurashi, Applications of nanotechnology in smart textile industry: a critical review, J. Adv. Res. 38 (2022) 55–75, https://doi.org/10.1016/j.jare.2022.01.008.
[2] B.S. Hassan, G.M.N. Islam, A. Haque, Applications of nanotechnology in textiles: a review, Adv. Res. Text. Eng. 4 (2019) 1038.
[3] B. Mahltig, Nanomaterials and textiles: review on materials and applications, J. Fiber Sci. Technol. 20 (2025) 1–15, https://doi.org/10.1177/15589250251318010.
[4] T.M. Abou Elmaaty, H. Elsisi, G. Elsayad, H. Elhadad, M.R. Plutino, Recent advances in functionalization of cotton fabrics with nanotechnology, Polymers 14 (2022) 4273, https://doi.org/10.3390/polym14204273.
[5] M.M. Rashid, B. Simončič, B. Tomšič, Recent advances in TiO_2-functionalized textile surfaces, Surf. Interfaces 22 (2021) 100890, https://doi.org/10.1016/j.surfin.2020.100890.
[6] A. Verbič, M. Gorjanc, B. Simončič, Zinc oxide for functional textile coatings: recent advances, Coatings 9 (2019) 550, https://doi.org/10.3390/coatings9090550.
[7] J. Vasiljević, I. Jerman, B. Simončič, Graphitic carbon nitride as a new sustainable photocatalyst for textile functionalization, Polymers 13 (2021) 2568, https://doi.org/10.3390/polym13152568.
[8] A.R. Gliga, S. Skoglund, I. Odnevall Wallinder, B. Fadeel, H.L. Karlsson, Size-dependent cytotoxicity of silver nanoparticles in human lung cells: the role of cellular uptake, agglomeration and Ag release, Part. Fibre Toxicol. 11 (2014) 11, https://doi.org/10.1186/1743-8977-11-11.
[9] N. Rahimi, R.A. Pax, E.M.A. Gray, Review of functional titanium oxides. I: TiO_2 and its modifications, Prog. Solid State Chem. 44 (2016) 86–105, https://doi.org/10.1016/j.progsolidstchem.2016.07.002.
[10] A.R. Khataee, M.B. Kasiri, Photocatalytic degradation of organic dyes in the presence of nanostructured titanium dioxide: influence of the chemical structure of dyes, J. Mol. Catal. A Chem. 328 (2010) 8–26, https://doi.org/10.1016/j.molcata.2010.05.023.
[11] M.R. Al-Mamun, S. Kader, M.S. Islam, M.Z.H. Khan, Photocatalytic activity improvement and application of UV-TiO_2 photocatalysis in textile wastewater treatment: a review, J. Environ. Chem. Eng. 7 (2019) 103248, https://doi.org/10.1016/j.jece.2019.103248.
[12] R. Katal, S. Masudy-Panah, M. Tanhaei, M.H.D.A. Farahani, H. Jiangyong, A review on the synthesis of the various types of anatase TiO_2 facets and their applications for photocatalysis, Chem. Eng. J. 384 (2020) 123384, https://doi.org/10.1016/j.cej.2019.123384.
[13] V. Etacheri, C. Di Valentin, J. Schneider, D. Bahnemann, S.C. Pillai, Visible-light activation of TiO_2 photocatalysts: advances in theory and experiments, J Photochem Photobiol C: Photochem Rev 25 (2015) 1–29, https://doi.org/10.1016/j.jphotochemrev.2015.08.003.
[14] S.K. Gaddam, R. Pothu, R. Boddula, Graphitic carbon nitride (g-C_3N_4) reinforced polymer nanocomposite systems—A review, Polym. Compos. 41 (2020) 430–442, https://doi.org/10.1002/pc.25410.
[15] S.T. Muntaha, J.A.S. Syed, M. Mateen, M.A. Shahzad, A. Parkash, A. Asrar, A. Emin, G.A. Ashraf, I. Ullah, M.A.F. Qaisar, S. Ali, A.M. Idris, Polymeric carbon nitride-based semiconductors as a beneficial candidate in photocatalysis diversity: a comprehensive review, Chem. Eng. J. 519 (2025) (2025) 165004, https://doi.org/10.1016/j.cej.2025.165004.
[16] G. Mamba, A.K. Mishra, Graphitic carbon nitride (g-C_3N_4) nanocomposites: a new and exciting generation of visible light driven photocatalysts for environmental pollution remediation, Appl. Catal. B: Environ. 198 (2016) 347–377, https://doi.org/10.1016/j.apcatb.2016.05.052.
[17] A. Sudhaik, P. Raizada, P. Shandilya, D.Y. Jeong, J.H. Lim, P. Singh, Review on fabrication of graphitic carbon nitride based efficient nanocomposites for photodegradation of aqueous phase organic pollutants, J. Ind. Eng. Chem. 67 (2018) 28–51, https://doi.org/10.1016/j.jiec.2018.07.007.
[18] S. Che, L. Zhang, T. Wang, D. Su, C. Wang, Graphitic carbon nitride-based photocatalysts for biological applications, Adv. Sustain. Syst. 6 (2022) 2100294, https://doi.org/10.1002/adsu.202100294.
[19] K. Gkini, I. Martinaiou, P. Falaras, A review on emerging efficient and stable perovskite solar cells based on g-C_3N_4 nanostructures, Materials 14 (2021) 2100294, https://doi.org/10.3390/ma14071679.
[20] D. Hao, J. Liu, H. Sun, B. Fu, J. Liu, J. Zhou, Integration of g-C_3N_4 into cellulose/graphene oxide foams for efficient photocatalytic Cr(VI) reduction, J. Phys. Chem. Solids 169 (2022) 110813, https://doi.org/10.1016/j.jpcs.2022.110813.
[21] M.G. Ashritha, K. Hareesh, A review on graphitic carbon nitride based binary nanocomposites as supercapacitors, J Energy Storage. 32 (2020) (2020) 101840, https://doi.org/10.1016/j.est.2020.101840.
[22] Q. Liang, B. Shao, S. Tong, Z. Liu, L. Tang, Y. Liu, M. Cheng, Q. He, T. Wu, Y. Pan, J. Huang, Z. Peng, Recent advances of melamine self-assembled graphitic carbon nitride-based materials: design, synthesis and application in energy and environment, Chem. Eng. J. 405 (2021) 126951, https://doi.org/10.1016/j.cej.2020.126951.
[23] J. Wang, S. Wang, A critical review on graphitic carbon nitride (g-C_3N_4)-based materials: preparation, modification and environmental application, Coord. Chem. Rev. 453 (2022) 214338, https://doi.org/10.1016/j.ccr.2021.214338.
[24] Y. Zheng, L. Lin, B. Wang, X. Wang, Graphitic carbon nitride polymers toward sustainable photoredox catalysis, Angew. Chem. Int. Ed. 127 (2015) 13060–13077, https://doi.org/10.1002/ange.201501788.
[25] X. Wang, S. Blechert, M. Antonietti, Polymeric graphitic carbon nitride for heterogeneous photocatalysis, ACS Catal. 2 (2012) 1596–1606, https://doi.org/10.1021/cs300240x.
[26] A. Akhundi, A. Badiei, G.M. Ziarani, A. Habibi-Yangjeh, M.J. Muñoz-Batista, R. Luque, Graphitic carbon nitride-based photocatalysts: toward efficient organic transformation for value-added chemicals production, Mol. Catal. 488 (2020) 110902, https://doi.org/10.1016/j.mcat.2020.110902.

[27] Q. Hao, G. Jia, W. Wei, A. Vinu, Y. Wang, H. Arandiyan, B.J. Ni, Graphitic carbon nitride with different dimensionalities for energy and environmental applications, Nano Res. 13 (2020) 18–37, https://doi.org/10.1007/s12274-019-2589-z.

[28] R.S. Chouhan, I. Jerman, D. Heath, S. Bohm, S. Gandhi, V. Sadhu, S. Baker, M. Hrovat, Emerging tri-s-triazine-based graphitic carbon nitride: a potential signal-transducing nanostructured material for sensor applications, Nano Select 2 (2021) 712–743, https://doi.org/10.1002/nano.202000228.

[29] L. Lu, Z. Lv, Y. Si, M. Liu, S. Zhang, Recent progress on band and surface engineering of graphitic carbon nitride for artificial photosynthesis, 462 (2018) 693–712. 10.1016/j.apsusc.2018.08.131.

[30] M. Jourshabani, B.K. Lee, Z. Shariatinia, From traditional strategies to z-scheme configuration in graphitic carbon nitride photocatalysts: recent progress and future challenges, Appl. Catal. B 276 (2020) 119157, https://doi.org/10.1016/j.apcatb.2020.119157.

[31] T. Kobkeatthawin, S. Chaveanghong, J. Trakulmututa, T. Amornsakchai, P. Kajitvichyanukul, S.M. Smith, Photocatalytic activity of TiO_2/g-C_3N_4 nanocomposites for removal of monochlorophenols from water, Nanomaterials 16 (2022) 2852, https://doi.org/10.3390/nano12162852.

[32] A.P. Shah, A.S. Sharma, V.S. Sharma, N.G. Shimpi, Polyacrylonitrile nanofibers incorporating Ag-decorated graphitic carbon nitride for the visible-light-activated selective oxidation of styrene, benzylic methylene groups, and benzene, Appl. Nano. Mater. 3 (2019) 1922–1933, https://doi.org/10.1021/acsanm.9b02559.

[33] S. Bayan, S. Pal, S. K. Ray, Interface engineered silver nanoparticles decorated g-C_3N_4 nanosheets for textile based triboelectric nanogenerators as wearable power sources, 94 (2022) 106928. 10.1016/j.nanoen.2022.106928.

[34] W. Li, H. Zhang, W. Chen, L. Yang, H. Wu, N. Mao, The effects of cotton cellulose on both energy band gap of g-C_3N_4–TiO_2 nanoparticles and enhanced photocatalytic properties of cotton-g-C_3N_4–TiO_2 composites, Cellul. 29 (2022) 193–212, https://doi.org/10.1007/s10570-021-04318-3.

[35] Y. Wang, X. Ding, P. Zhang, Q. Wang, K. Zheng, L. Chen, J. Ding, X. Tian, X. Zhang, Convenient and recyclable TiO_2/g-C_3N_4 photocatalytic coating: layer-by-layer self-assembly construction on cotton fabrics leading to improved catalytic activity under visible light, Ind. Eng. Chem. Res. 58 (2019) 3978–3987, https://doi.org/10.1021/acs.iecr.8b05509.

[36] Y. Chen, W. Lu, H. Shen, Y. Gu, T. Xu, Z. Zhu, G. Wang, W. Chen, Solar-driven efficient degradation of emerging contaminants by g-C_3N_4-shielding polyester fiber/TiO_2 composites, Appl. Catal. B 258 (2019) 117960, https://doi.org/10.1016/j.apcatb.2019.117960.

[37] Q. Xiong, Y. Chen, T. Xu, Z. Zhu, W. Chen, W. Lu, Highly efficient purification of emerging pollutants and bacteria in natural water by g-C_3N_4-sheltered fibers containing TiO_2, Appl. Surf. Sci. 559 (2021) 149839, https://doi.org/10.1016/j.apsusc.2021.149839.

[38] Y. Yang, C. Lu, J. Ren, X. Li, Y. Ma, W. Huang, X. Zhao, Enhanced photocatalytic hydrogen evolution over TiO_2/g-C_3N_4 2D heterojunction coupled with plasmon Ag nanoparticles, Ceram. Int. 46 (2020) 5725–5732, https://doi.org/10.1016/j.ceramint.2019.11.021.

[39] S. Ghafoor, A. Inayat, F. Aftab, H. Duran, K. Kirchhoff, S. Waseem, S.N. Arshad, TiO_2 nanofibers embedded with g-C_3N_4 nanosheets and decorated with Ag nanoparticles as Z-scheme photocatalysts for environmental remediation, J. Environ. Chem. Eng. 7 (2019) 103452, https://doi.org/10.1016/j.jece.2019.103452.

[40] C. Wang, Z. Rao, A. Mahmood, X. Wang, Y. Wang, X. Xie, J. Sun, Improved photocatalytic oxidation performance of gaseous acetaldehyde by ternary g-C_3N_4/Ag-TiO_2 composites under visible light, J. Colloid Interface Sci. 602 (2021) 699–711, https://doi.org/10.1016/j.jcis.2021.05.186.

[41] Y. Chen, W. Huang, D. He, Y. Situ, H. Huang, Construction of heterostructured g-C_3N_4/Ag/TiO_2 microspheres with enhanced photocatalysis performance under visible-light irradiation, ACS Appl. Mater. Interfaces 6 (2014) 14405–14414, https://doi.org/10.1021/am503674e.

[42] R. Geng, J. Yin, J. Zhou, T. Jiao, Y. Feng, L. Zhang, Y. Chen, Z. Bai, Q. Peng, In situ construction of Ag/TiO_2/g-C_3N_4 heterojunction nanocomposite based on hierarchical co-assembly with sustainable hydrogen evolution, Nanomaterials 10 (2020) 1, https://doi.org/10.3390/nano10010001.

[43] C.J. Van Oss, R.F. Giese, Z. Li, et al., Determination of contact angles and pore sizes of porous media by column and thin layer wicking, J. Adhesion Sci. Technol. 6 (4) (1992) 413–428.

[44] E. Chibowski, F. González-Caballero, Theory and practice of thin-layer wicking, Langmuir 9 (1993) 330–340.

[45] M. Karkare, The direct transition and not indirect transition, is more favourable for band gap calculation of anatase TiO_2 nanoparticles, Int. J. Sci. Eng. Res. 6 (2015) 48–53.

[46] S.P. Sun, C.J. Li, J.H. Sun, S.H. Shi, M.H. Fan, Q. Zhou, Decolorization of an azo dye Orange G in aqueous solution by Fenton oxidation process: effect of system parameters and kinetic study, J. Hazard. Mater. 161 (2009) 1052–1057, https://doi.org/10.1016/j.jhazmat.2008.04.080.

[47] T. Tomašegović, S. Mahović Poljaček, I. Jurišić, D. Donevski, Fine-tuning flexographic ink's surface properties and providing anti-counterfeit potential via the addition of TiO_2 and ZnO nanoparticles, Micro 5 (2025) 20, https://doi.org/10.3390/micro5020020.

[48] J. Sehnert, K. Baerwinkel, J. Senker, Ab initio calculation of solid-state NMR spectra for different triazine and heptazine based structure proposals of g-C_3N_4, J. Phys. Chem. B 111 (2007) 10671–10680, https://doi.org/10.1021/jp072001k.

[49] Y. Hu, Y. Shim, J. Oh, S. Park, S. Park, Y. Ishii, Synthesis of 13C-,15N-labeled graphitic carbon nitrides and NMR-based evidence of hydrogen-bonding assisted two-dimensional assembly, Chem. Mat. 29 (2017) 5080–5089, https://doi.org/10.1021/acs.chemmater.7b00069.

[50] W. Li, Z. Guo, L. Jiang, L. Zhong, G. Li, J. Zhang, K. Fan, S. Gonzalez-Cortes, K. Jin, C. Xu, T. Xiao, P.P. Edwards, Facile: In situ reductive synthesis of both nitrogen deficient and protonated g-C_3N_4 nanosheets for the synergistic enhancement of visible-light H_2 evolution, Chem. Sci. 11 (2020) 2716–2728, https://doi.org/10.1039/c9sc05060d.

[51] Z. Jin, Q. Zhang, J. Chen, S. Huang, L. Hu, Y.J. Zeng, H. Zhang, S. Ruan, T. Ohno, Hydrogen bonds in heterojunction photocatalysts for efficient charge transfer, Appl. Catal. B 234 (2018) 198–205, https://doi.org/10.1016/j.apcatb.2018.04.057.

[52] T. Katan, R. Kargl, T. Mohan, T. Steindorfer, M. Mozetič, J. Kovač, K. Stana Kleinschek, Solid phase peptide synthesis on chitosan thin films, Biomacromolecules 23 (2022) 731–742, https://doi.org/10.1021/acs.biomac.1c01155.

[53] A.W. Jatoi, I.S. Kim, Q.Q. Ni, Cellulose acetate nanofibers embedded with AgNPs anchored TiO_2 nanoparticles for long term excellent antibacterial applications, Carbohydr. Polym. 207 (2019) 640–649, https://doi.org/10.1016/j.carbpol.2018.12.029.

[54] J. Žigon, J. Kovač, M. Petrič, The influence of mechanical, physical and chemical pre-treatment processes of wood surface on the relationships of wood with a waterborne opaque coating, Prog. Org. Coat. 162 (2022) 106574, https://doi.org/10.1016/j.porgcoat.2021.106574.

[55] Z. Moridi Mahdieh, S. Shekarriz, F. Afshar Taromi, M. Montazer, A new method for in situ synthesis of Ag–TiO_2 nanocomposite particles on polyester/cellulose fabric by photoreduction and self-cleaning properties, Cellul. 25 (2018) 2355–2366, https://doi.org/10.1007/s10570-018-1694-6.

[56] A.O. Özdemir, B. Caglar, O. Çubuk, F. Coldur, M. Kuzucu, E.K. Guner, B. Doğan, S. Caglar, K.V. Özdokur, Facile synthesis of TiO_2-coated cotton fabric and its versatile applications in photocatalysis, pH sensor and antibacterial activities, Mater. Chem. Phys. 287 (2022) 126342, https://doi.org/10.1016/j.matchemphys.2022.126342.

[57] M. Michalska, V. Matějka, J. Pavlovský, P. Praus, M. Ritz, J. Serenčíšová, L. Gembalová, M. Kormunda, M. Foniok, M. Reli, G., Simha Martynková, effect of Ag modification on TiO_2 and melem/g-C_3N_4 composite on photocatalytic performances, Sci. Rep. 13 (2023) 5270.

[58] J. Ran, H. Chen, S. Bi, Q. Guo, C. Yan, X. Tang, D. Cheng, G. Cai, X. Wang, Polydopamine-induced in-situ growth of zeolitic imidazolate framework-8/TiO_2 nanoparticles on cotton fabrics for photocatalytic performance, Prog. Org. Coat. 152 (2021) (2021) 106123, https://doi.org/10.1016/j.porgcoat.2020.106123.

[59] K.H. Leong, S.L. Liu, L.C. Sim, P. Saravanan, M. Jang, S. Ibrahim, Surface reconstruction of titania with g-C_3N_4 and Ag for promoting efficient electrons migration and enhanced visible light photocatalysis, Appl. Surf. Sci. 358 (2015) 370–376, https://doi.org/10.1016/j.apsusc.2015.06.184.

[60] G. Socrates, Infrared and Raman Characteristic Group Frequencies: Tables and Charts, John Wiley & Sons, 2001.

[61] J. Široký, R.S. Blackburn, T. Bechtold, J. Taylor, P. White, Attenuated total reflectance Fourier transform Infrared spectroscopy analysis of crystallinity changes in lyocell following continuous treatment with sodium hydroxide, Cellul. 17 (2010) 103–115, https://doi.org/10.1007/s10570-009-9378-x.

[62] B. Tomšič, V. Jovanovski, B. Orel, M. Mihelčič, J. Kovač, V. Francetič, B. Simončič, Bacteriostatic photocatalytic properties of cotton modified with TiO_2 and TiO_2/aminopropyltriethoxysilane, Cellul. 22 (2015) 3441–3463, https://doi.org/10.1007/s10570-015-0696-x.

[63] M.M. Rashid, B. Tomšič, B. Simončič, I. Jerman, D. Štular, M. Zorc, N.Č. Korošin, In situ tailoring of Ag-doped-TiO_2/TPMP/cotton nanocomposite with UV-protective, self-sterilizing and flame-retardant performance for advanced technical textiles, Polym. Degrad. Stab. 216 (2023) 110504, https://doi.org/10.1016/j.polymdegradstab.2023.110504.

[64] W. Bahloul, V. Bounor-Legaré, G. Seytre, P. Cassagnau, Influence of a non-polar medium (alkane and molten polypropylene) on the titanium n-butoxide hydrolysis-condensation reactions, J. Solgel. Sci. Technol. 57 (2011) 86–94, https://doi.org/10.1007/s10971-010-2327-1.

[65] B. Tomšič, M. Blagojevič, N. Klančar, E. Makoter, K. Močenik, N. Pirš, S. Šmid, M. Veskova, M. Gorjanc, M. Kert, B. Simončič, Multifunctional properties of cotton fabric tailored via green synthesis of TiO_2/curcumin composite, Tekstilec 68 (2025) 82–99. 10.14502/tekstilec.68.2024135.

[66] W. Li, R. Liang, A. Hu, Z. Huang, Y.N. Zhou, Generation of oxygen vacancies in visible light activated one-dimensional iodine TiO_2 photocatalysts, RSC Adv. 4 (2014) 36959–36966, https://doi.org/10.1039/c4ra04768k.

[67] Q. Huang, J. Yu, S. Cao, C. Cui, B. Cheng, Efficient photocatalytic reduction of CO_2 by amine-functionalized g-C_3N_4, Appl. Surf. Sci. 358 (2015) 350–355, https://doi.org/10.1016/j.apsusc.2015.07.082.

[68] T. Alizadeh, S. Nayeri, N. Hamidi, Graphitic carbon nitride (g-C_3N_4)/graphite nanocomposite as an extraordinarily sensitive sensor for sub-micromolar detection of oxalic acid in biological samples, RSC Adv. 9 (2019) 13096–13103, https://doi.org/10.1039/c9ra00982e.

[69] D. Štular, E. Savio, B. Simončič, M. Šobak, I. Jerman, I. Poljanšek, A. Ferri, B. Tomšič, Multifunctional antibacterial and ultraviolet protective cotton cellulose developed by in situ biosynthesis of silver nanoparticles into a polysiloxane matrix mediated by sumac leaf extract, Appl. Surf. Sci. 563 (2021) 150361, https://doi.org/10.1016/j.apsusc.2021.150361.

[70] E.K. Kambale, C.I. Nkanga, B.P.I. Mutonkole, A.M. Bapolisi, D.O. Tassa, J.M. I. Liesse, R.W.M. Krause, P.B. Memvanga, Green synthesis of antimicrobial silver nanoparticles using aqueous leaf extracts from three Congolese plant species (Brillantaisia patula, Crossopteryx febrifuga and Senna siamea), Heliyon 6 (2020) e04493, https://doi.org/10.1016/j.heliyon.2020.e04493.

[71] A. Javed, J. Wiener, A. Tamulevičienė, T. Tamulevičius, A. Lazauskas, J. Saskova, S. Račkauskas, One step in-situ synthesis of zinc oxide nanoparticles for multifunctional cotton fabrics, Materials 14 (2021) 3956, https://doi.org/10.3390/ma14143956.
[72] X. Sun, N. Talha, A.M. Ahmed, M.A. Rafea, N.A. Alenazi, M.R. Abukhadra, Steric and energetic studies on the influence of cellulose on the adsorption effectiveness of Mg trapped hydroxyapatite for enhanced remediation of chlorpyrifos and omethoate pesticides, Int. J. Biol. Macromol. 265 (2024) 130711, https://doi.org/10.1016/j.ijbiomac.2024.130711.
[73] M. Thommes, K. Kaneko, A.V. Neimark, J.P. Olivier, F. Rodriguez-Reinoso, J. Rouquerol, K.S.W. Sing, Physisorption of gases, with special reference to the evaluation of surface area and pore size distribution (IUPAC Technical Report), Pure Appl. Chem. 87 (2015) 1051–1069, https://doi.org/10.1515/pac-2014-1117.
[74] Y. Zhang, T. Mori, J. Ye, M. Antonietti, Phosphorus-doped carbon nitride solid: Enhanced electrical conductivity and photocurrent generation, J. Am. Chem. Soc. 132 (2010) 6294–6295, https://doi.org/10.1021/ja101749y.
[75] A. Mills, S. Le Hunte, An overview of semiconductor photocatalysis, J. Photochem. Photobiol. A Chem. 108 (1997) 1–35.
[76] M. Pelaez, N.T. Nolan, S.C. Pillai, M.K. Seery, P. Falaras, A.G. Kontos, P.S. M. Dunlop, J.W.J. Hamilton, J.A. Byrne, K. O'Shea, M.H. Entezari, D.D. Dionysiou, A review on the visible light active titanium dioxide photocatalysts for environmental applications, Appl. Catal. B 125 (2012) 331–349, https://doi.org/10.1016/j.apcatb.2012.05.036.
[77] X. Wang, K. Maeda, A. Thomas, K. Takanabe, G. Xin, J.M. Carlsson, K. Domen, M. Antonietti, A metal-free polymeric photocatalyst for hydrogen production from water under visible light, Nat. Mater. 8 (2009) 76–80, https://doi.org/10.1038/nmat2317.
[78] J. Liu, Y. Liu, N. Liu, Y. Han, X. Zhang, H. Huang, Y. Lifshitz, S.-T. Lee, J. Zhong, Z. Kang, Metal-free efficient photocatalyst for stable visible water splitting via a two-electron pathway, Science 347 (2015) 970–974, https://doi.org/10.1126/science.aaa3145.
[79] K. Wu, J. Chen, T. Lian, Efficient hot-electron transfer by a plasmon-induced interfacial charge-transfer transition, Science 349 (2015) 632–635, https://doi.org/10.1126/science.aac544.
[80] S. Mubeen, J. Lee, N. Singh, S. Kraemer, An autonomous photosynthetic device in which all charge carriers derive from surface plasmons, Nat. Nanotechnol. 8 (2013) 247–251, https://doi.org/10.1038/NNANO.2013.18.
[81] X. Chen, S.S. Mao, Titanium dioxide nanomaterials: Synthesis, properties, modifications and applications, Chem. Rev. 107 (2007) 2891–2959, https://doi.org/10.1021/cr0500535.
[82] J. Zhang, M. Zhang, R.-Q. Sun, X. Wang, A facile band alignment of polymeric carbon nitride semiconductors to construct isotype heterojunctions, Angew. Chem. Int. Ed. 124 (2012) 10292–10296, https://doi.org/10.1002/ange.201205333.
[83] T. Sharifi, Y. Ghayeb, T. Mohammadi, M.M. Momeni, Enhanced photoelectrochemical water splitting of CrTiO$_2$ nanotube photoanodes by the decoration of their surface via the photodeposition of Ag and Au, Dalton Trans. 47 (2018) 11593, https://doi.org/10.1039/c8dt02383b.
[84] V. Kavaliūnas, P. Čeplikas, M. Sriubas, G. Laukaitis, The sensitization of TiO$_2$ thin film by Ag nanoparticles for the improvement of photocatalytic efficiency, Appl. Sci. (Switzerland) 12 (2022) 5725, https://doi.org/10.3390/app12115725.
[85] M. Sorvali, T. Tinus, J. Thamby, M. Honkanen, H. Ali-Löytty, A. Charmforoushan, M. Valden, J.J. Saarinen, J.M. Mäkelä, Silver nanoparticle coatings with adjustable extinction spectra produced with liquid flame spray, and their role in photocatalytic enhancement of TiO$_2$, Mater. Des. 239 (2024) 112800, https://doi.org/10.1016/j.matdes.2024.112800.
[86] T. Žigon, Preparation of finish on cellulose fibres with nanoparticles of titanium dioxide, silver and graphitic carbon nitride with antimicrobial and photocatalytic performance, University of Ljubljana Faculty of Natural Sciences and Engineering (2022).
[87] A. Salinaro, A.V. Emeline, J. Zhao, H. Hidaka, V.K. Ryabchuk, N. Serpone, Terminology, relative photonic efficiencies and quantum yields in heterogeneous photocatalysis. Part II: Experimental determination of quantum yields, Pure Appl. Chem. 71 (1999) 321–335.
[88] N. Serpone, A. Salinaro, Terminology, relative photonic efficiencies and quantum yields in heterogeneous photocatalysis. Part I: Suggested protocol, Pure Appl. Chem 71 (1999) 303–320.
[89] J. Yu, S. Wang, J. Low, W. Xiao, Enhanced photocatalytic performance of direct Z-scheme g-C$_3$N$_4$-TiO$_2$ photocatalysts for the decomposition of formaldehyde in air, Phys. Chem. Chem. Phys. 15 (2013) 16883–16890, https://doi.org/10.1039/c3cp53131g.
[90] Q. Xu, L. Zhang, J. Yu, S. Wageh, A.A. Al-Ghamdi, M. Jaroniec, Direct Z-scheme photocatalysts: principles, synthesis, and applications, Mater. Today 21 (2018) 1042–1063, https://doi.org/10.1016/j.mattod.2018.04.008.
[91] H. Li, Y. Gao, X. Wu, P.-H. Lee, K. Shih, Fabrication of heterostructured g-C$_3$N$_4$/Ag-TiO$_2$ hybrid photocatalyst with enhanced performance in photocatalytic conversion of CO$_2$ under simulated sunlight irradiation, Appl. Surf. Sci. 402 (2017) 198207.
[92] J. Low, J. Yu, M. Jaroniec, S. Wageh, A.A. Al-Ghamdi, Heterojunction photocatalysts, Adv. Mater. 29 (2017) 1601694, https://doi.org/10.1002/adma.201601694.
[93] J. Chandrasekar, M. Venkatesan, J.H. Lin, C.C. Kuo, Purification of water using TiO$_2$/g-C$_3$N$_5$ nanocomposite: a visible light assisted photocatalytic activity, Z. Phys. Chem. 238 (2024) 1931–1941, https://doi.org/10.1515/zpch-2023-0560.
[94] S. Huang, J. Zhong, J. Li, J. Chen, Z. Xiang, W. Hu, M. Li, Z-scheme TiO$_2$/g-C$_3$N$_4$ composites with improved solar-driven photocatalytic performance deriving from remarkably efficient separation of photo-generated charge pairs, Mater. Res. Bull. 84 (2016) 65–70, https://doi.org/10.1016/j.materresbull.2016.07.036.
[95] A. Salleh, R. Naomi, N.D. Utami, A.W. Mohammad, E. Mahmoudi, N. Mustafa, M. B. Fauzi, The potential of silver nanoparticles for antiviral and antibacterial applications: a mechanism of action, Nanomaterials 10 (2020) 1566–1586, https://doi.org/10.3390/nano10081566.
[96] P.V. Laxma Reddy, B. Kavitha, P.A. Kumar Reddy, K.H. Kim, TiO$_2$-based photocatalytic disinfection of microbes in aqueous media: a review, Environ. Res. 154 (2017) 296–303, https://doi.org/10.1016/j.envres.2017.01.018.
[97] C. Regmi, B. Joshi, S.K. Ray, G. Gyawali, R. Pandey, Understanding mechanism of photocatalytic microbial decontamination of environmental wastewater, Front. Chem. 6 (2018) 33, https://doi.org/10.3389/fchem.2018.00033.
[98] J. Zhen, A. Sun, L. Yang, R. Wang, M. Liu, Y. Liu, W. Zhang, Silver-conjugated-polyarginine anchored cotton fabrics exhibit durable and efficient antimicrobial properties, ACS Omega 10 (2025) 34822–34830, https://doi.org/10.1021/acsomega.5c03854.
[99] W. Guoa, W. Liub, L. Xuc, P. Fenga, Y. Zhangc, W. Yanga, C. Shuaia, Halloysite nanotubes loaded with nano silver for the sustained-release of antibacterial polymer nanocomposite scaffolds, J. Mater. Sci. Technol. 46 (2020) 237–247.